

AD-A131 966

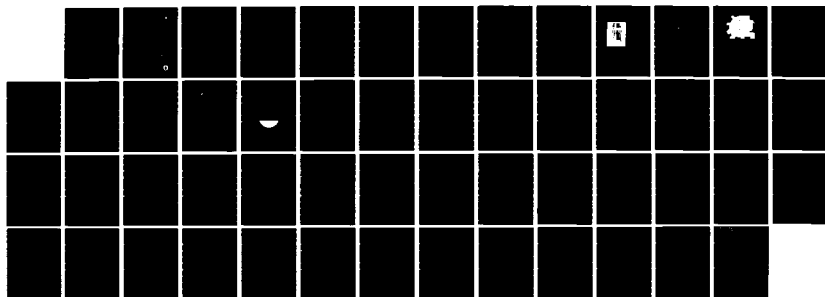
THE FAR INFRARED SKY SURVEY EXPERIMENT(U) AIR FORCE
GEOPHYSICS LAB HANSCOM AFB MA S D PRICE ET AL.
18 FEB 83 AGGL-TR-83-0055

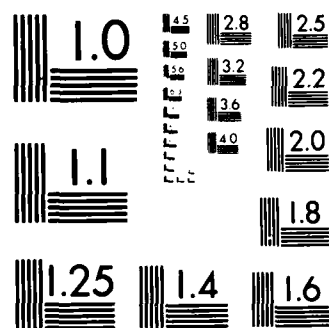
1/1

UNCLASSIFIED

F/G 17/5

NL

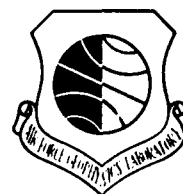




MICROCOPY RESOLUTION TEST CHART
NATIONAL BUREAU OF STANDARDS-1963 A

AD A131966

AFGL-TR-83-0055
ENVIRONMENTAL RESEARCH PAPERS, NO. 826

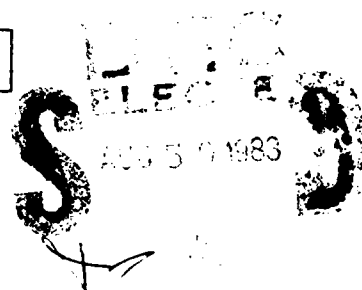


The Far Infrared Sky Survey Experiment Final Report

STEPHAN D. PRICE
THOMAS L. MURDOCK
KANDIAH SHIVANANDAN

18 February 1983

Approved for public release; distribution unlimited.



OPTICAL PHYSICS DIVISION
AIR FORCE GEOPHYSICS LABORATORY
HANSCOM AFB, MASSACHUSETTS 01731

PROJECT 7670

AIR FORCE SYSTEMS COMMAND, USAF

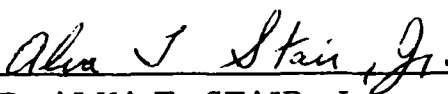


DTIC FILE COPY

83 08 23 065

This report has been reviewed by the ESD Public Affairs Office (PA)
and is releasable to the National Technical Information Service (NTIS).

This technical report has been reviewed and
is approved for publication.


DR. ALVA T. STAIR, Jr.
Chief Scientist

Qualified requestors may obtain additional copies from the
Defense Technical Information Center. All others should apply
to the National Technical Information Service.

Unclassified

SECURITY CLASSIFICATION OF THIS PAGE (When Data Entered)

REPORT DOCUMENTATION PAGE		READ INSTRUCTIONS BEFORE COMPLETING FORM
1. REPORT NUMBER AFGL-TR-83-0055	2. GOVT ACCESSION NO.	3. RECIPIENT'S CATALOG NUMBER
4. TITLE (and Subtitle) THE FAR INFRARED SKY SURVEY EXPERIMENT FINAL REPORT		5. TYPE OF REPORT & PERIOD COVERED Scientific. Interim.
7. AUTHOR(s) Stephan D. Price Thomas L. Murdock Kandiah Shivanandan		6. PERFORMING ORG. REPORT NUMBER ERP, No. 826
9. PERFORMING ORGANIZATION NAME AND ADDRESS Air Force Geophysics Laboratory (OPI) Hanscom AFB Massachusetts 01731		8. CONTRACT OR GRANT NUMBER(s)
11. CONTROLLING OFFICE NAME AND ADDRESS Air Force Geophysics Laboratory (OPI) Hanscom AFB Massachusetts 01731		10. PROGRAM ELEMENT, PROJECT, TASK AREA & WORK UNIT NUMBERS 62101F 76700609
14. MONITORING AGENCY NAME & ADDRESS (if different from Controlling Office)		12. REPORT DATE 18 February 1983
		13. NUMBER OF PAGES 52
		15. SECURITY CLASS. (of this report) Unclassified
		15a. DECLASSIFICATION DOWNGRADING SCHEDULE
16. DISTRIBUTION STATEMENT (of this Report) Approved for public release; distribution unlimited.		
17. DISTRIBUTION STATEMENT (of the abstract entered in Block 20, if different from Report)		
18. SUPPLEMENTARY NOTES Naval Research Laboratory, Washington, DC 20375		
19. KEY WORDS (Continue on reverse side if necessary and identify by block number) Infrared Celestial backgrounds HII regions		
20. ABSTRACT (Continue on reverse side if necessary and identify by block number) Approximately 9000 square degrees of the celestial sphere was surveyed in four infrared bands with a rocket-probe-borne telescope. This Far Infrared Sky Survey Experiment (FIRSSE) covered the galactic plane between 120° and 255° longitude and the Orion and Taurus Molecular Clouds. A list of almost 300 bright 90 μm sources is presented along with associated measurements at 20, 27 and 40 μm. A description is given of the conduct of the experiment, the first space-borne use of super-fluid helium under active thermal loading.		

DD FORM 1 JAN 73 1473 EDITION OF 1 NOV 65 IS OBSOLETE

SECURITY CLASSIFICATION OF THIS PAGE (When Data Entered)

Dist	Spec
A	

Preface

The Far Infrared Sky Survey Experiment (FIRSSE) was the first successful use of super-fluid helium as a cryogen under active thermal loading on a spaceborne experiment. This single experiment surveyed more area of sky than all the previous balloon and aircraft measurements combined. The successful performance of an experiment as complex and innovative as FIRSSE is a cooperation effort of many individuals, too numerous to be mentioned here. However, the outstanding effort of key people must be acknowledged. Eban Hiscock and Chris Krebs of the AFGL research rocket branch directed the pre-flight integration and the field support. Stewart Lyons of Space Vector was responsible for the attitude control system and in-flight maneuvers. Jim Lester and Ron Pearson directed the design and construction of the sensor cryogenic system at Ball Aerospace Systems Divisions (BASD) and provided integration and field support. Special thanks to Dick Herring of BASD for his interest in the experiment, especially during the lean periods.

The focal plane and signal processing electronics were designed, built and tested by Santa Barbara Research Center under the supervision of Don Campbell. Randy Tate of NRL provided extensive assistance in the laboratory calibration and field testing of the focal plane and sensor. With able support from Paul Cucchiaro, Dave Akerstrom was the key individual for the design and construction of the ground support system, and the field support for the sensor especially for the super-fluid helium transfer. Wentworth Institute built the payload under the guidance of Ed LeBlanc. Tom Campbell and Larry Smart insured that the payload performed as designed.

Data processing was in the capable hands of Len Marcotte. Paul LeVan performed the necessary calculations for the in-flight calibration.

Contents

1. INTRODUCTION	7
2. INSTRUMENTATION	8
3. THE EXPERIMENT	15
4. IN-FLIGHT PERFORMANCE	18
5. THE DATA	27
6. DATA REDUCTION - CALIBRATION	33
7. DATA REDUCTION	35
8. THE FIRSSE LONG WAVELENGTH CATALOG	37
REFERENCES	51

Illustrations

1. The FIRSSE Optical Bench	9
2. An Exploded View of the FIRSSE Focal Plane	10
3. Face-on View of the FIRSSE Focal Plane Showing the Aperture Mask and Location of the Arrays	11
4. Cutaway View of the FIRSSE Telescope	13
5. Launch Configuration for FIRSSE	15
6. Configuration of FIRSSE During Data Acquisition	16

Illustrations

7. The Survey Scan Pattern	17
8. Temperature Profile During Flight	20
9. Temperature Profile During Flight	20
10. Temperature Profile During Flight	21
11. RMS Noise for the 20 μ m Channels During Data Acquisition	23
12. RMS Noise for the 27 μ m Channels During Data Acquisition	24
13. RMS Noise for the 94 μ m Channels During Data Acquisition	25
14. RMS Noise for the 40 μ m Channels During Data Acquisition	26
15. Transit and Signals From NGC 2170	28
16. Transit and Signals From NGC 2183 and 2171	29
17. Signals From Optical Contamination	30
18. Response From an Extended Source of Nearly Constant Brightness	31
19. Signals From Saturn	32
20. Data Acquisition for the Experiment	35
21. Flow Chart for Reduction of the Data and Association With Known Sources	36
22. Detailed Flow Chart of Reduction Procedures for Obtaining a List of Sources	38
23. Aitoff Projection of the FIRSSE Coverage and Sources Detected at 93 μ m	40

Tables

1. System Parameters for FIRSSE	14
2. Table of Observations	41

The Far Infrared Sky Survey Experiment

Final Report

I. INTRODUCTION

The Far Infrared Sky Survey Experiment (FIRSSE) is a joint effort between the Air Force Geophysics Laboratory (AFGL) and the Naval Research Laboratory (NRL) to survey the sky in five broad spectral bands between 8 and 120 μ m. Technical direction for the design and construction of the dewar and integration of the sensor at Ball Aerospace Systems Division and the focal plane array with signal processing electronics at the Santa Barbara Research Center was provided by both AFGL and NRL. Payload development and fabrication was AFGL's responsibility as well as the field preparation and launch. The detailed data reduction and analysis for all detectors was done by AFGL, with NRL independently selecting long wavelength sources by visual inspection.

The flight took place on 22 January 1982 from the White Sands Missile Range, New Mexico at 8^h00^m00^s.191 GMT. The ARIES guided rocket lifted the 660-kg payload to a 379-km peak altitude for a total of 450 sec of data acquisition. The success of this experiment marks the first use of super-fluid helium and porous plug containment on a space borne experiment under dynamic external thermal loading.

During the flight about 9000 square degrees were surveyed (21 percent of the sky) with at least 80 percent overlap. The scans covered about 100° of galactic longitude along the anticenter region of the plane as well as a large area of

(Received for publication

Gould belt. Several hundred sources were detected in one or more of the spectral bands. The bright 100- μ m sources have a high degree of association with HII region while fainter 100- μ m emission was detected from the brighter stars and asteroids. The survey appears complete down to 100 Jansky (Jy) at 100 μ m.

The advantages of an exo-atmospheric infrared experiment are obvious. The atmosphere absorbs infrared radiation and is opaque at certain wavelengths; beyond 35 μ m for example. Elevating the observing platform by aircraft and balloon reduces this problem but structure in the thermal emission from the atmosphere limit the field of view and/or sensitivity of the measurement. Not only are atmospheric problems eliminated in space but the telescope can be cryogenically cooled to the point where self emission does not limit the sensitivity of a detector even for large fields of view.

Several early rocket-borne celestial survey experiments were attempted^{1, 2} with ambiguous results. The Cornell group^{3, 4, 5} succeeded in obtaining 100- μ m measurements on several HII regions with a rocketborne instrument. These experiments used normal fluid helium as a cryogen as super-fluid could not be maintained or contained during preflight and flight conditions. Thus the 100- μ m Ge:Ga detectors were not as sensitive as the Ge bolometers later flown on balloon and aircraft. With the advent of Ge:xx, long wavelength photoconductors^{6, 7, 8} with high frequency response and good NEP's and sintered Nickel porous plugs for super-fluid containment, a rocket-borne survey instrument becomes competitive with the longer duration balloon flights in obtaining long wavelength observations ($30 \mu\text{m} < \lambda < 120 \mu\text{m}$) at medium ($10'$) spatial resolution.

2. INSTRUMENTATION

The instrument and experiment have been described by Price, Murdock and Shivanandan.⁹ We augment that description in this section and discuss the performance of the instrument. The FIRSSE optical system was built by Perkin Elmer Corporation as a demonstration of technical capability. A comparable instrument, SPICE, was also successfully flown on 15 September 1982 by AFGL as a complementary survey to that performed by the short wavelength arrays in FIRSSE.

The FIRSSE optical system (Figure 1) is a doubly folded Gregorian design and has a spherical primary 36 cm in diameter. Spherical aberration and coma are corrected to first order by aspherized secondary and tertiary mirrors. The folding flat is located at the intermediate focal plane and doubles as a field stop. The $f/2.4$ system has a focal length of 86.4 cm. The focal plane is convex and covers a

(Due to the large number of references cited above, they will not be listed here. See References, page 51.)

22.5 field of view with a 4' mm plate scale. The linear obscuration of the secondary housing is 0.48 for a total collecting area of 750 cm^2 . The optical bench is an integrated system made of beryllium. The secondary is cantilevered by four beryllium rods which pass through the primary mirror and are attached to the optics support fixture.

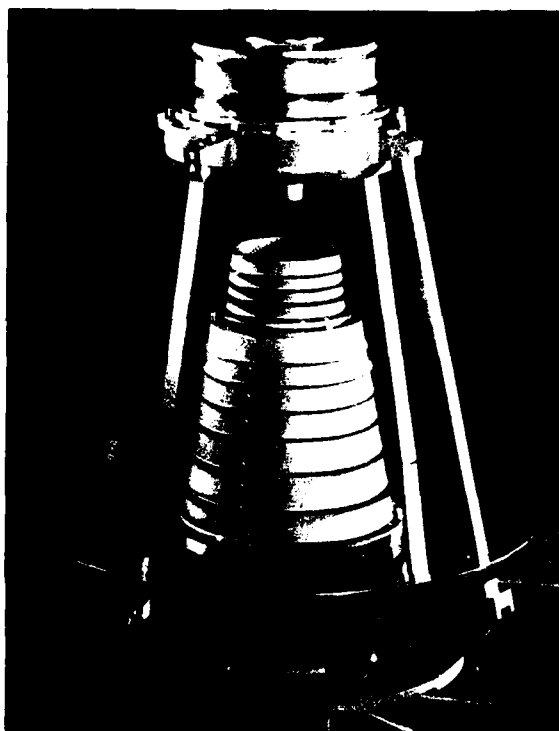


Figure 1. The FIRSSE Optical Bench

The focal plane (Figures 2 and 3) is modular in design. The mechanical housing and array supports are made of beryllium for thermal compatibility with the optical system. Two thin film resistors are mounted above the focal plane, one each on either side. These resistors are heated by a precisely controlled voltage, flooding the focal plane with thermal photons and stimulating the detectors as a check on their working status. The equal intensity effective wavelength and bandwidth together with measured NEFD and other pertinent data are listed in Table 1 for each of the five arrays. Measurements at the Naval Ocean Systems Center¹⁰ on the filter-detector combinations provide the values in the first four bands.

10. NOSC (1980) Test Data on SBRC FIRSSE Focal Plane Array, Infrared Devices Branch, Electronic Materials Sciences Division, Naval Ocean Systems Center, San Diego, CA 92152, May 1980.

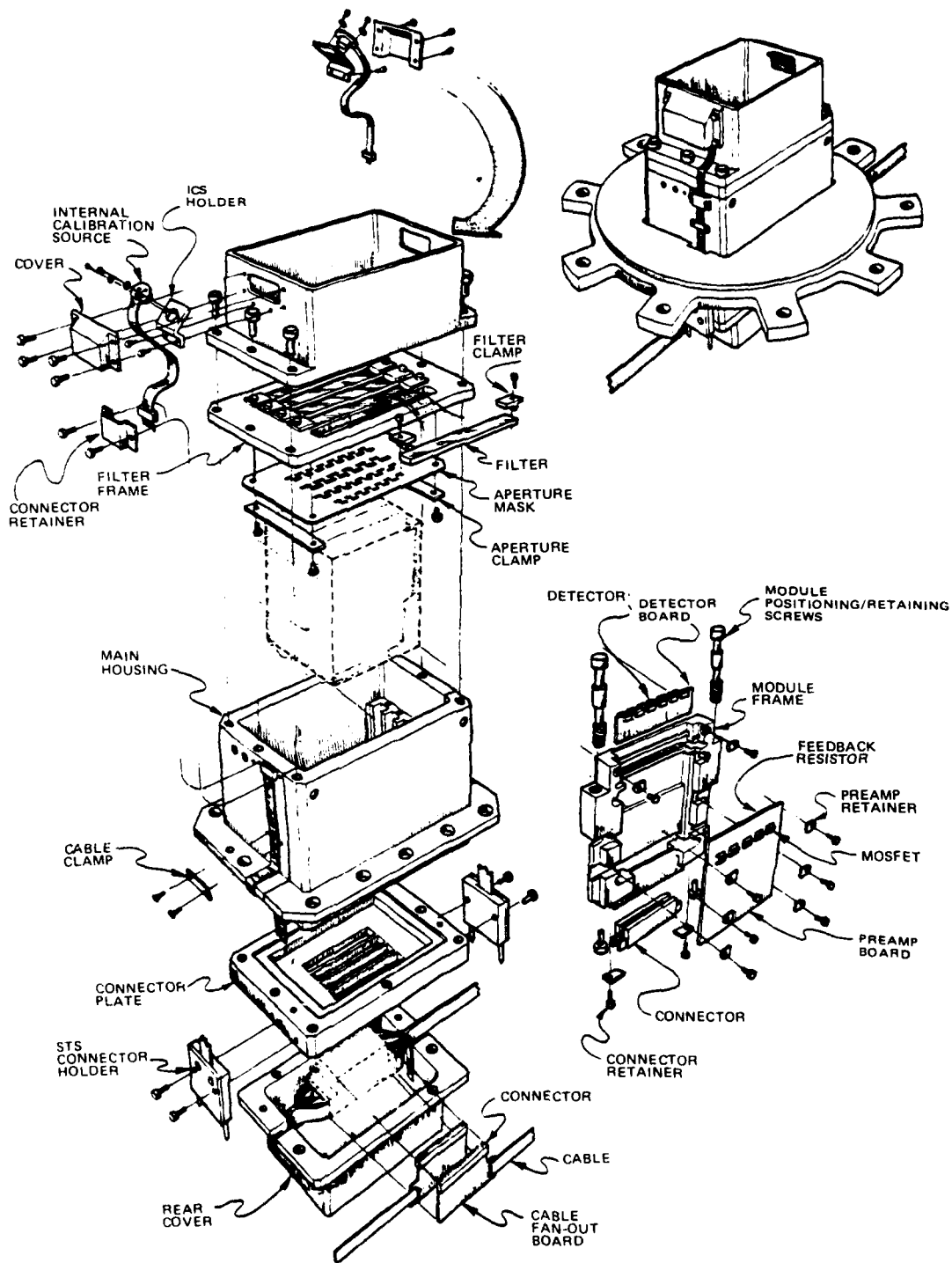


Figure 2. An Exploded View of the FIRSSE Focal Plane

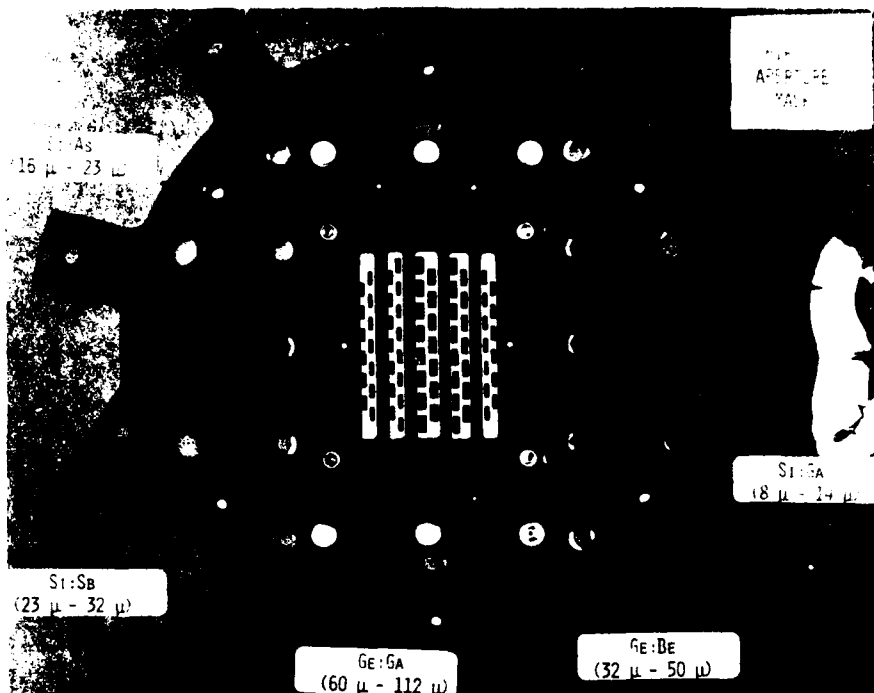


Figure 3. Face-on View of the FIRSSE Focal Plane Showing the Aperture Mask and Location of the Arrays

The Ge:Ga detector response and transmission of the 100- μ m filter were obtained by NRL and convolved for the effective wavelength and bandwidth; the NEP is from the final SBRC tests. The last column lists the NEFD determined from the in-flight calibration.

Several anomalies showed up during construction and testing of the focal plane array. The thermal conductivity of the beryllium housing is very low at temperatures of 2 to 3° K. Consequently, self heating from the MOSFETS raised the temperature of the Ge:Ga detectors above 4.5° K which is above their operating temperature. This problem was solved by carefully heat sinking the long wavelength arrays. The Si:xx detectors perform better at higher temperatures and the thermal isolation was retained for these arrays. In the final configuration the Ge:Ga and Ge:Be arrays ran at 2.5° K, 0.3 K above the 2.2° K temperature of the dewar cooling ring while the Si:xx arrays were at 5.0° K. A minimum of spiking was observed on the silicon arrays of these temperatures under optimum biases.

The trade-off for warmer silicon array temperatures was that the load resistor values were about half (3.5×10^9 ohms) that of the Ge:xx arrays. Additional stray

capacitance had to be introduced into the preamplifier circuit in order to reduce the frequency of the roll-off in the boost of the trans-impedance amplifier. This was necessary in order to prevent aliasing unwanted high frequency noise by the sampling and digitizing of the data stream by the pulse code modulator (PCM).

The focal plane array was placed into the optical system such that the two outer, short wavelength arrays were at best focus. The depth of field for the curved focal plane was sufficient to cause no degradation in the amount of energy on the larger detectors.

A cutaway of the sensor is shown in Figure 4. The instrument is cooled from a 17-liter dewar. A sintered nickel porous plug with a $10\text{-}\mu\text{m}$ pore size acts as a phase separator in the dewar vent line to contain super-fluid helium. The optics, focal plane, inner radiation shield, and background plate are conductively cooled through the inner cooling ring on the dewar. The vapor shield is cooled by vent gas from the dewar and, in turn, conductively cools the cover vapor shield. Straps of 0.99999 pure aluminum are used to provide good thermal conductivity to the focal plane, the secondary mirror and support structure, and along the inner radiation shield. The heat leak is relatively low, 0.56 W, with the focal plane contributing less than 1% to this total. The background plate in the sensor cover ran warmer, 19K, than the 15K design goal. Although the background plate is gold-plated to reduce emissivity, the photon flux at the detectors in the 70- to $120\text{-}\mu\text{m}$ band is still high, $\sim 10^{10}$ phot. $\text{cm}^{-2} \text{sec}^{-1}$, at this temperature. This is 1.5 to 2 orders of magnitude higher than was anticipated through the side lobe response of the instrument during flight. The biases of the Ge:Ga had to be reduced in order for them to operate at this background. Thus the average NEP derived from the SBRC data for the Ge:Ga array and listed in Table 1 were increased by roughly a factor of 2 before flight.

A specially designed 250-liter dewar and transfer system is used to fill the FIRSSE dewar with liquid helium at a temperature 2.7 to 3K just above the λ point. About two liters of helium are pumped away in cooling the instrument to 1.7 - 1.8K or 7.9 torr static vapor pressures. Hold time, defined as the time from closing the helium vent line to the time the helium in the dewar goes through the λ point transition, in excess of 100 min were achieved.

Safety considerations require that payload personnel vacate the tower for final arming at least 30 min before launch. The helium vent is closed 55 min before launch to leave enough time to remove the vent pump, install the access panel, and remove the clean bags around the payload. The super-fluid helium is unvented until $T + 90$ sec when it is opened to the vacuum of space through a solenoid valve.

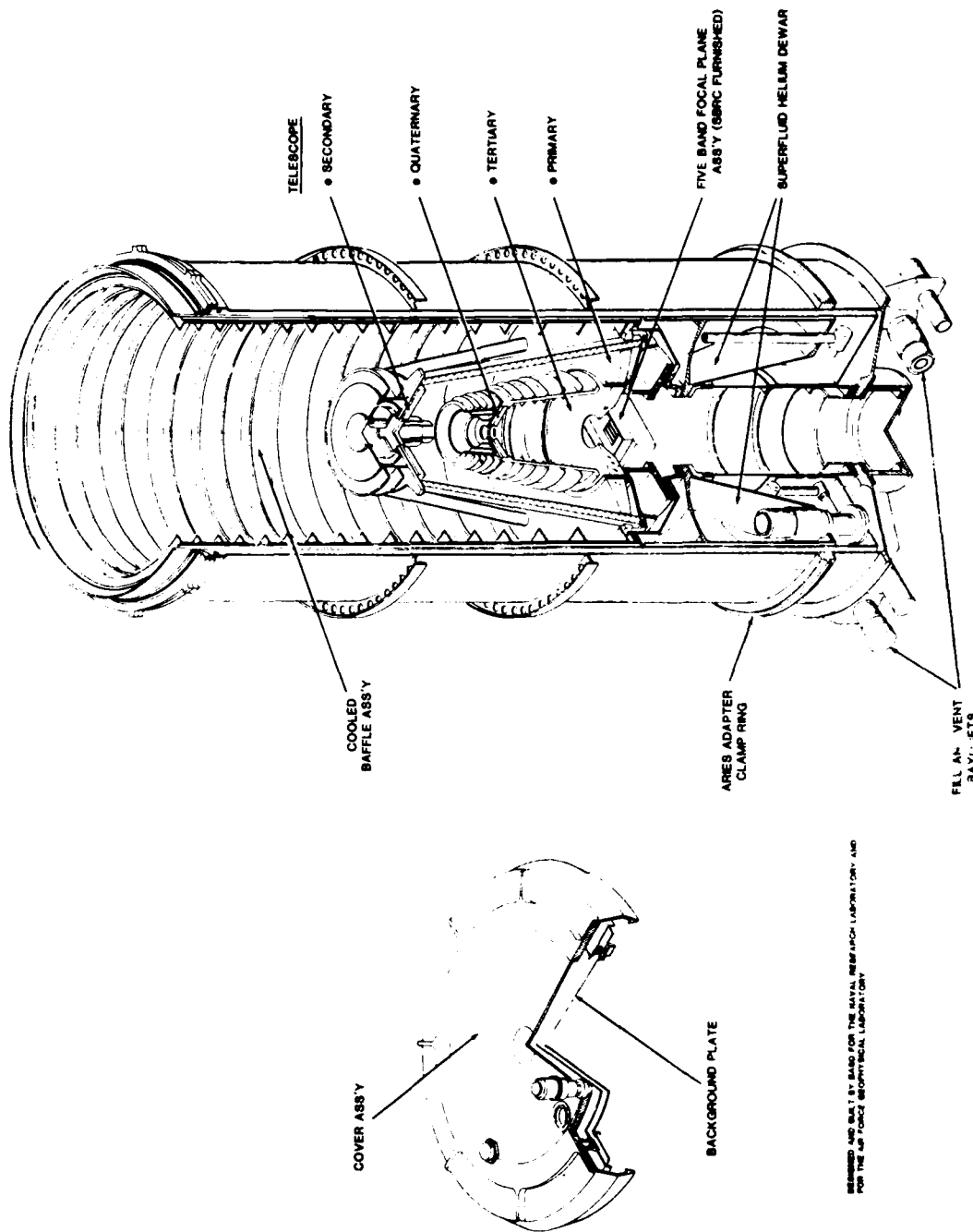


Figure 4. (b) away View of the FIRSSI Telescope

Table 1. System Parameters for FIRSSE

Band (50% Response)	Detectors No.	Material	Size	λ_e (μm)	$\Delta\lambda$ (μm)	NEFD Calc-2 $\times 10^{-17} \text{ W cm}^{-2}$	In-Flight NEFD $\times 10^{-17} \text{ W cm}^{-2}$	Jy
8.2 μm - 13.8 μm	13	Si:Ga	2:5 \times 10'	11.2	4.5	1.5 \pm 0.2	--	
16.7 μm - 23.4 μm	13	Si:As	2:5 \times 10'	20.3	4.2	0.5 \pm 0.1	2	4
23.6 μm - 30.3 μm	15	Si:Sb	2:5 \times 10'	27.3	4.9	0.9 \pm 0.3	4	15
34 μm - 50 μm	15	Ge:Be	4:0 \times 12'	40.0	17.9	5.0 \pm 0.1	40	120
65 μm - 117 μm	15	Ge:Ga	5:3 \times 12'	93.7	41.4	0.3 \pm 0.2	2	15

3. THE EXPERIMENT

The payload is a cone/cylinder in shape, 3.9 m long and 0.9525 m in diameter. It is divided into three sections: an aspect section containing the star mapper and a BASD large lens STRAP star tracker, an instrument compartment with the telescope and payload electronics, and the attitude control system and recovery package in the nose cone. The launch configuration is shown schematically in Figure 5. Figure 6 depicts the payload during data taking.

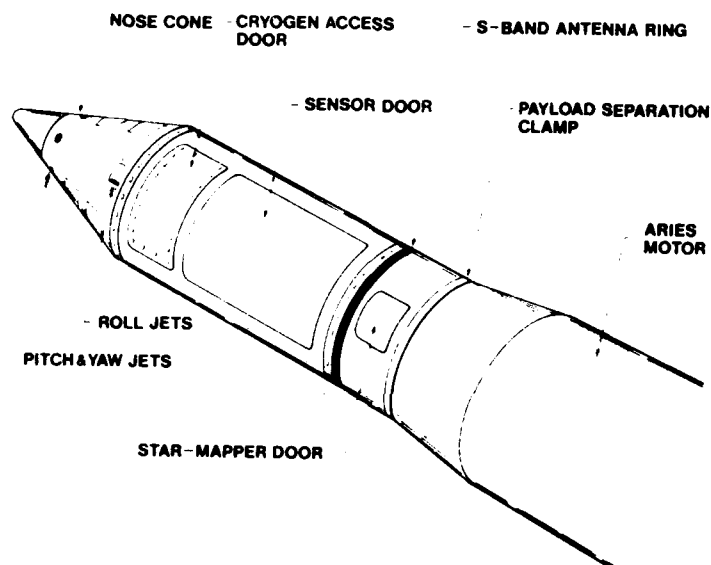


Figure 5. Launch Configuration for FIRSSE

Powered flight lasts about 62 sec. After an 18-sec coast period, manacle clamps holding the payload and vehicle together are released and a pneumatic bellows separates the two at a relative velocity of 8.75 m/sec. After separation the motor is spun about the longitudinal axis to provide dynamic stability to keep the motor nozzles pointed away from the payload. These steps are taken to prevent the optical contamination seen on other experiments¹¹ from the smoldering

11. Price, S. D., Murdock, T. L., McIntyre, A., Huffman, R. E., and Paulsen, D. E. (1980) On the diffuse cosmic ultraviolet background measured from ARIES A-8, Astrophys. J. Letters, 240:L.

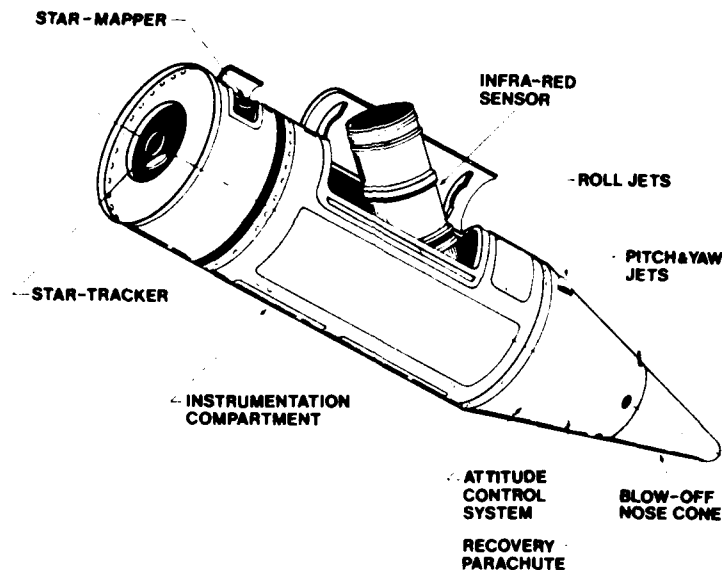


Figure 6. Configuration of FIRSSE During Data Acquisition

residual fuel and butyl rubber liner in the spent motor. The payload is cleaned during the preflight preparation as described by Price, Cunniff and Walker¹² to eliminate optical contamination by dust and other particles.

After separation the payload is pitched over 180° and maneuvered to bring the optical axis of the star tracker to the direction of a star. The launch time and star are selected such that the star is at meridian transit near the zenith. This choice produces the least off-axis radiation into the telescope from the earth. During preflight alignment¹³ the null position of the optical axis of the tracker was accurately co-aligned with the geometric roll axis of the payload. The payload was spin balanced to bring the dynamic roll axis into near coincidence with the geometric roll axis. Once the star is acquired in the tracker 6° field-of-view, control of the pitch and yaw jets is transferred to the tracker. Error signals due to deviations of the star from tracker null are used by the attitude control system to drive the payload roll axis to the coordinates of the star and to maintain that position throughout the flight.

12. Price, S.D., Cunniff, C.V., and Walker, R.W. (1978) Cleanliness Consideration for the AFGL Infrared Celestial Survey Experiments, AFGL-TR-78-0171, AD A060116.

13. Price, S.D., Akerstrom, D.A., Cunniff, C.V., Marcotte, L.P., Tandv, P.C., and Walker, R.G. (1978) Aspect Determination for the AFGL Infrared Celestial Survey Experiments, AFGL-TR-78-0253, AD A067017.

The star mapper, star tracker, and payload doors are unlatched and opened during the pitchover maneuver. The sensor cover is removed and the telescope deployed while the star tracker acquires the star. The payload is spun about the roll axis causing the sensor focal plane to sweep out a band along a small circle centered on the pole star one focal plane array high as shown in Figure 7. The zenith angle is stepped 2.14° at the completion of a 382.5° roll. The roll rate is changed during each step to compensate for the cosecant z distortion in the scan geometry, and to maintain a constant linear scan rate of $20^\circ/\text{sec}$. Maximum deployment of 71.5° occurs near peak altitude when the earth's horizon is at the maximum depression angle of 19° . The sensor is subsequently stepped up during the down leg portion of the flight. This profile results in the largest areal coverage for a given constraint due to the off-axis performance of the telescope.

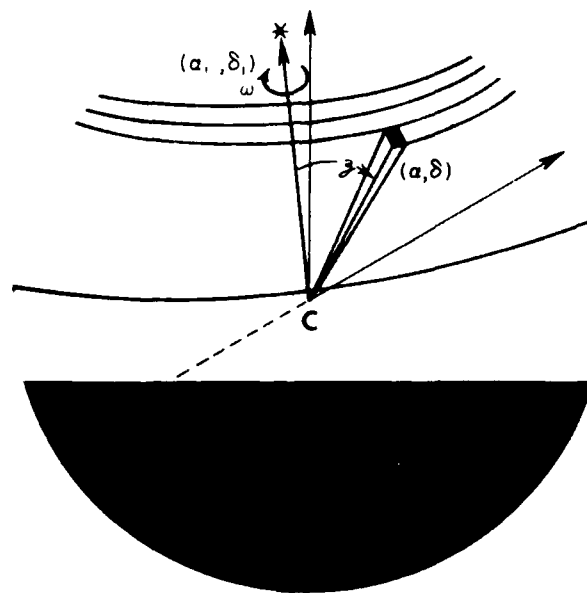


Figure 7. The Survey Scan Pattern. The pole rotation is fixed to a star with celestial coordinates (α_1, δ_1) . The payload is rotated at an angular rate, ω , and the sensor deployed to a zenith angle z . Bottom scan line represents the maximum deployment consistent with OAR constraints. The shaded area at the bottom is section of sky obscured by the earth during the experiment. Shaded area around the south pole is the sky unreachable from White Sands Missile Range

As shown in Figure 7, the pole of rotation is accurately fixed to the inertial coordinates of the star. The sensor deployment gimbal is orthogonal to the roll axis. A 13-bit shaft encoder reads the deployment angle to 1' accuracy. The geometry is an alt-azimuth system with the star at the pole. Azimuth is determined by stellar transits observed by a small visual photometer through an "N" slit reticle mask. Azimuth reference was carefully aligned during preflight integration to the deployment plane of the telescope.

At the end of the flight, the telescope is stowed, the cap replaced and the doors closed to protect the various sensors from re-entry heating. The parachute deployment is activated at an altitude of 3 km by a barometer switch. The payload was recovered in excellent condition.

4. IN-FLIGHT PERFORMANCE

All detectors worked well during flight except those at $11\ \mu\text{m}$. A bias short to shield ground on the focal plane connector to the $11\ \mu\text{m}$ array resulted in no observations at this wavelength. The measurements made with the Ge:xx arrays were degraded for about half the flight as explained below.

The temperature profiles for the various monitors in the sensor are shown in Figures 8, 9 and 10. The location of these monitors are defined in the figure legends.

All temperature monitors are nominal until the cover is removed. A thermal pulse of about 40 W from the payload structure is seen by the instrument as the cap is removed and the sensor deployed at about 96 secs. This pulse raises temperatures throughout the telescope. About 8 W of aperture loading is experienced at the first deployment angle. This is almost equally divided between contributions from the payload and earth. As the deployment angle of the telescope increases the contribution from the earth dominates, peaking to 11 W at maximum deployment. The thermal loading profile reverses as the telescope is stepped up. This profile is best reflected by the aperture temperature shown in Figure 8. This monitor is located at the front end of the inner radiation shield and is most sensitive to external thermal input. The small amplitude cyclic structure reflects the change in solid angle subtended by the earth during a roll due to the pole star not being at local zenith.

Blade No. 2 is located about 4 cm down from the front aperture on the outside of the second baffle blade. The temperature profile for this monitor mirrors that of the aperture but with smaller amplitude and considerable smoothing. This temperature difference is primarily due to the fact that the baffle blades are more directly coupled to the cooling ring through 0.0009 pure aluminum straps than the

radiation shield. The baffle blades and radiation shield are tied to the primary mirror and helium tank at the same point. The relative stability of the blade No. 2 temperature from 100 to 160 sec is probably caused by the primary mirror absorbing some of the heat and warming up.

A more disastrous consequence of this thermal loading is that the focal plane warms up, as profiled in Figure 9. The temperature monitor for the focal plane is located in the middle of the Ge:Ga array. The variation generally correlates with the helium tank monitor on the cooling ring. The focal plane is strapped to the ring at four points and therefore averages the temperature variations around the ring. The helium tank monitor is sensitive to a localized change of temperature on the cooling ring. The variations probably indicate how well the super-fluid helium wets the tank nearest the monitor.

These profiles can be explained as follows: the aperture loading changes from 8 to 11 W during the flight and is primarily due to the earth. This heat is put into the helium dewar at or very near the cooling ring with some of the load taken up by the thermal inertia of the optics. The heat causes local instabilities in the super-fluid helium wetting the walls nearest to the cooling ring. As the super-fluid is driven away from a specific area on the tank that area warms then subsequently cools when the super-fluid again wets that locale on the dewar. The four cooling straps to the focal plane average these local variations. Unfortunately, the focal plane temperature exceeded the maximum operating value of 4.3 K for the Ge:xx arrays about 20% of the data acquisition time. Another 30% of the time the temperature was above 3.9 K, the point at which the Ge:xx array have responsivities degraded by about a factor of two.

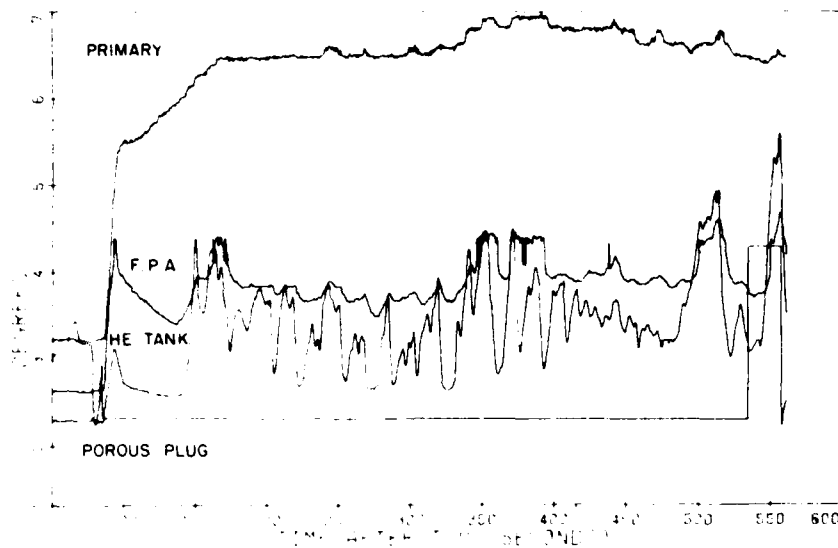


Figure 8. Temperature Profile During Flight. The aperture monitor is at the front end of the inner radiation shield; Blade 2 is about 4 cm from the front end of the inner radiation shield; primary is on the back of the primary mirror; He tank is on the cooling ring on the bottom of the helium dewar

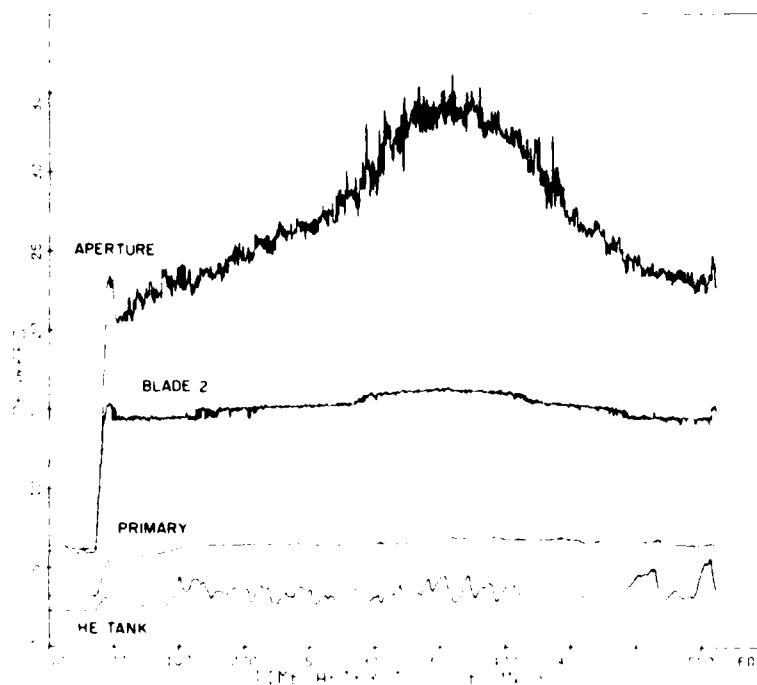


Figure 9. Temperature Profile During Flight. The F. P. A. monitor is in the middle on the front surface of the Ge:Ga array

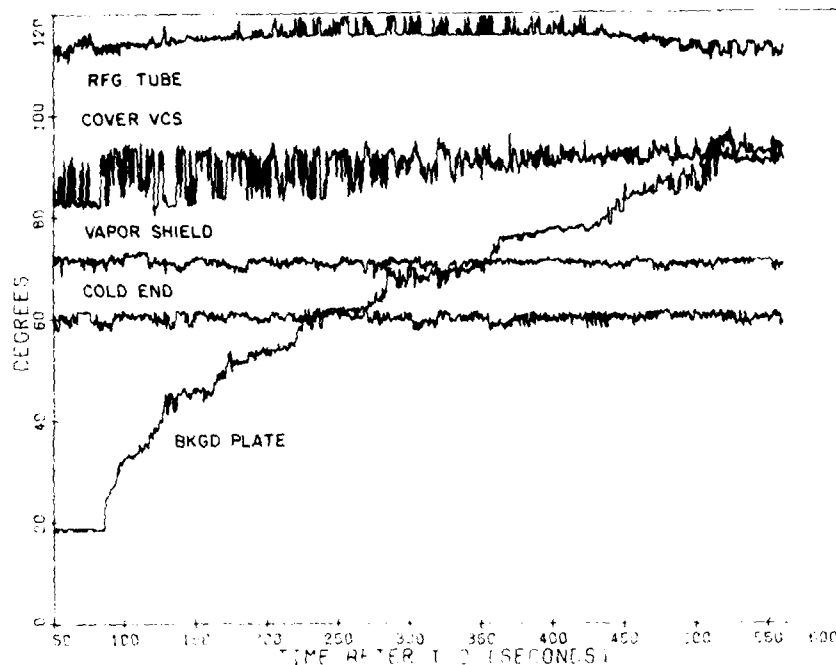


Figure 10. Temperature Profile During Flight. Background plate monitor is on the back surface of the center of the background plate. Cold end is the cooling post to which the vapor shield is tied; vapor shield is several cm from the end of the vapor shield; cover VCS is in the center of the cover vapor shield; Rfg tube is the outer cooling station

The in-flight performance of the detectors is graphically depicted in Figures 11, 12, 13 and 14 which show the root mean square (rms) values of the noise for the detectors in the 17-23 μm , 24-30 μm , 65-117 μm , and 34-50 μm bands respectively. The noise was smoothed over an interval of 0.72 sec. The elevated noise in the Si:xx bands (Figures 11 and 12) occupies, at most, 10% of the data acquisition time and is due almost entirely to particulate contamination. Except for the beginning of data acquisition when the background may be increased by outgassing from the payload and the periods of contamination, the noise levels for the silicon arrays are constant. Thus, the off-axis rejection of the instrument was sufficiently high to maintain preamplifier noise limited performance on these detectors throughout the entire flight.

The noise performance of the Ge:Ga detectors in Figure 13 show several effects. The brief periods of contamination show up at the same time they were observed in the silicon arrays. The general trend in noise follows the temperature of the focal plane array. The times when the focal plane array temperature was greater than 4°K (150-170 sec, 350-360 sec, 370-395 sec, 490-510 sec) are also times when the noise is highest. This correlation is best seen by comparing detector 13 in Figure 13 with the focal plane array temperature profile in Figure 9. The times when the noise falls rapidly to a value near zero followed by an equally rapid increase are times when the detector temperatures were at the operating limit and the detector-preamplifier is either locked up or turned off.

The porous plug and helium tank temperature plus the helium tank pressure indicate that super-fluid helium was successfully contained in the dewar until T + 535 sec. The super-fluid could have been maintained longer under this thermal load if a porous plug of larger surface area was used to allow a higher flow rate for the vapor. The super-fluid helium did wet the walls of the dewar as anticipated. Fully half the flight returned high quality data in the long wavelength arrays, especially the 100 μ m array of Ge:Ga detectors (see Figure 13). As complete redundancy was planned for these arrays, a survey with good sensitivity was performed over the area scanned with degraded confirming observations.

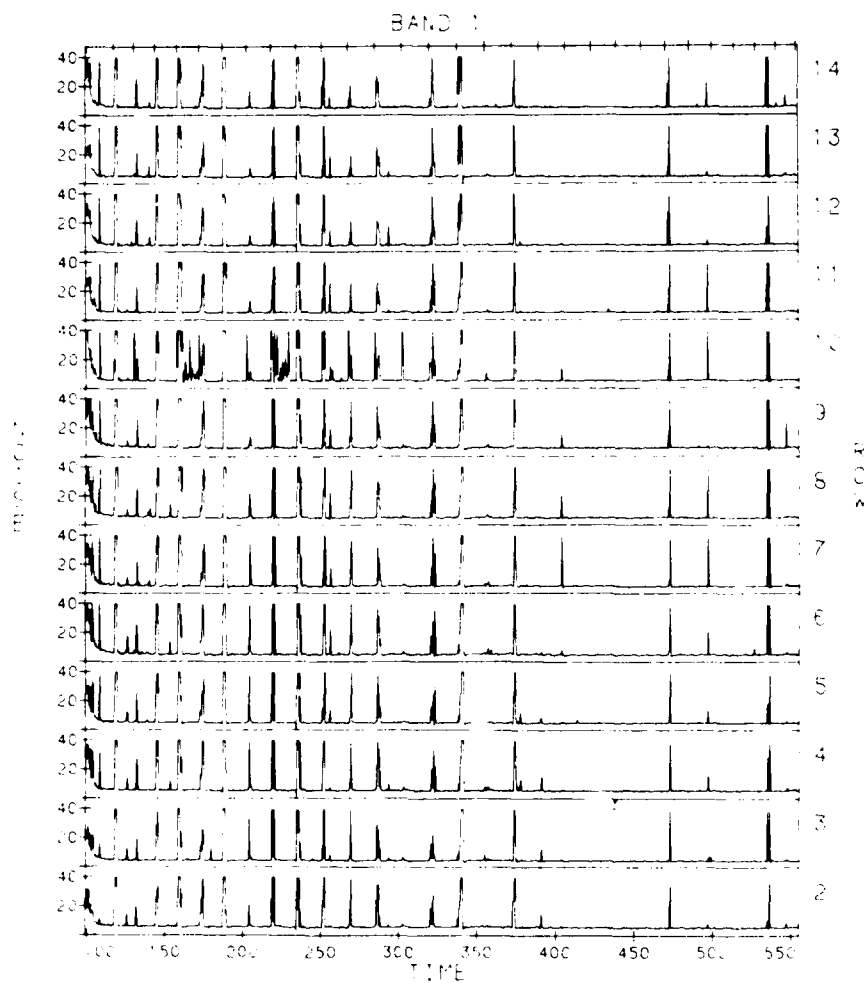


Figure 11. RMS Noise for the 20 μ m Channels During Data Acquisition

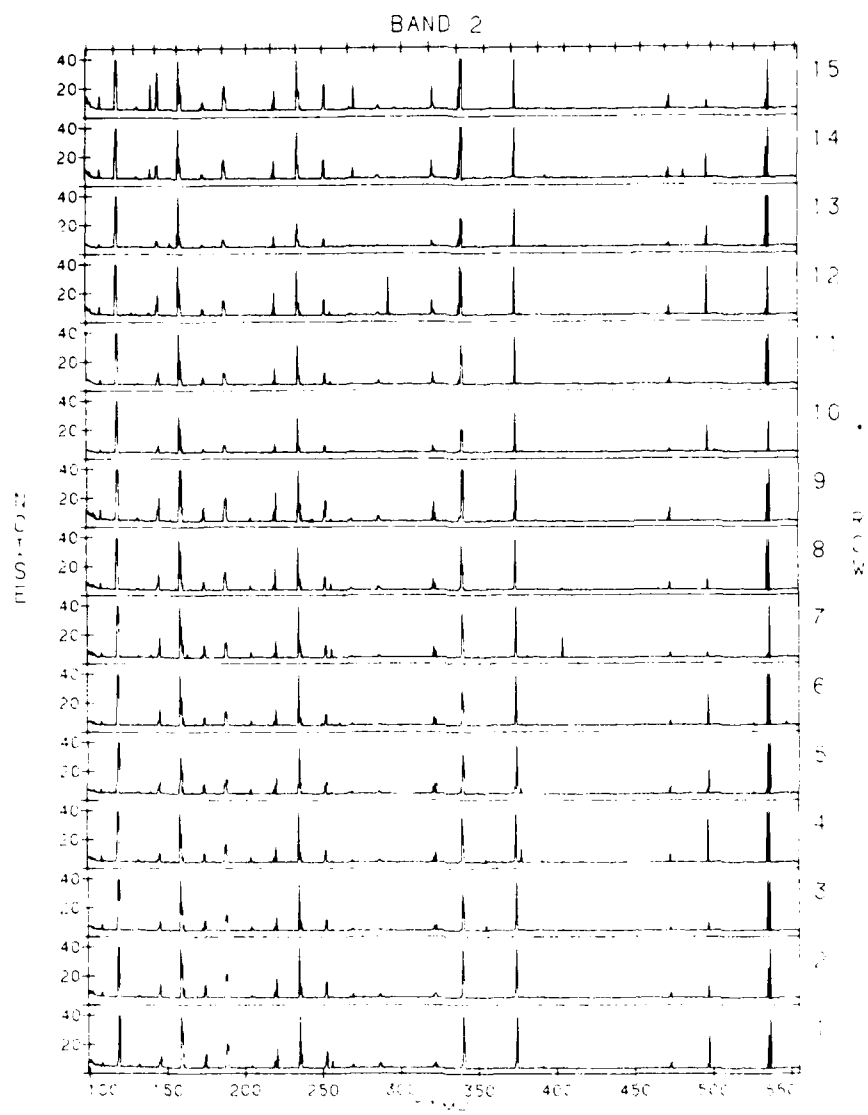


Figure 12. RMS Noise for the 27 μm Channels During Data Acquisition

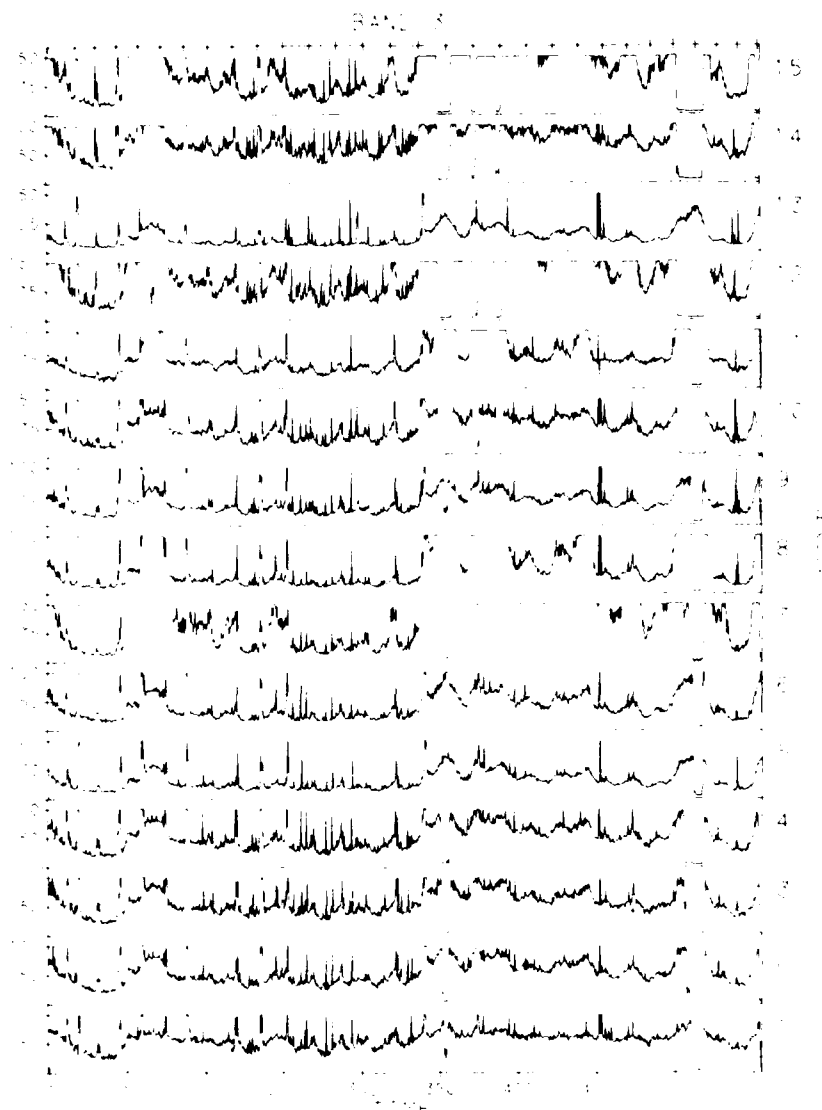


Figure 13. RMS Noise for the 94 μ mChannels During Data Acquisition



Figure 14. RMS Noise for the 40 μ m Channels During Data Acquisition

5. THE DATA

Examples of various aspects of the data during the flight are shown in Figures 15 through 19. The detection of NGC 2170 (= AFGL 877) is shown in the center of Figure 15, NGC 2183 (= AFGL 890S) and NGC 2071 (= AFGL 818) in Figure 16. The high pass filtering in the signal processing electronics produces a negative undershoot which follows the positive signal from a source. A first order zero (RC differentiator) with a characteristic frequency of 10 Hz is used for the ac coupling. The signal should asymptotically recover to zero for such a filter. The positive overshoot in Figure 15 for the top trace is due to the signal saturating the electronics and subsequent memory loss of the signal train. The objects in Figures 15 and 16 are somewhat extended but are obviously quite cold. The data in Figures 15 and 16 are different traces taken at about the same time when the focal plane temperature was about 3.9° K. Note the noise levels are different for the 100 μ m detectors in these figures.

Examples of optical contamination are shown in Figures 17 and 18. A near field dust particle would produce a doughnut shaped out-of-focus image¹² for the Gregorian optical system with its central obscuration. A detector scanning the center of the image produces a characteristic double peaked signal as seen in Figure 17. If the scan is away from the image hole produced by the central obscuration, the detector sees an extended source of constant brightness. The ac coupling in the electronics produces an extended signal as the leading edge of the image is detected. This is followed by a gradual decay to zero as the filter (differentiator) takes out the low frequency background. A negative signal occurs when the detector moves off the image as seen in Figure 18.

Figure 19 contains the signature of Saturn. At this time the focal plane temperature is 4.4° K. The resistance of the Ge:Ga detectors has dropped below the value of the load resistor and the bias seen by the detector through the transimpedance amplifier is reversed; thus the signals are negative. The Ge:Be detector on the bottom trace has completely turned off. Although the Ge:Be detector on the top trace is still responsive the temperature variation on the focal plane produces a large amplitude base line drift.

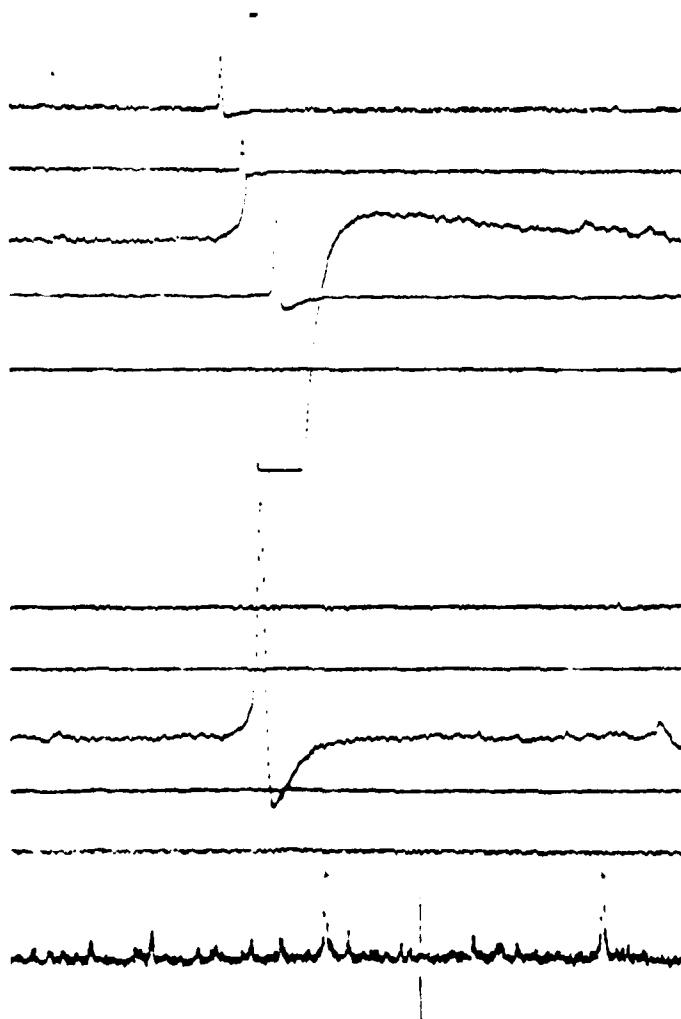


Figure 15. Transit and Signals From NGC 2170. The detectors are arranged sequentially in the order shown in Figure 3; 20, 27, 90, 40 and 11 μm respectively. The staggered output is the time delay due to the offset of the individual detectors in the focal plane.

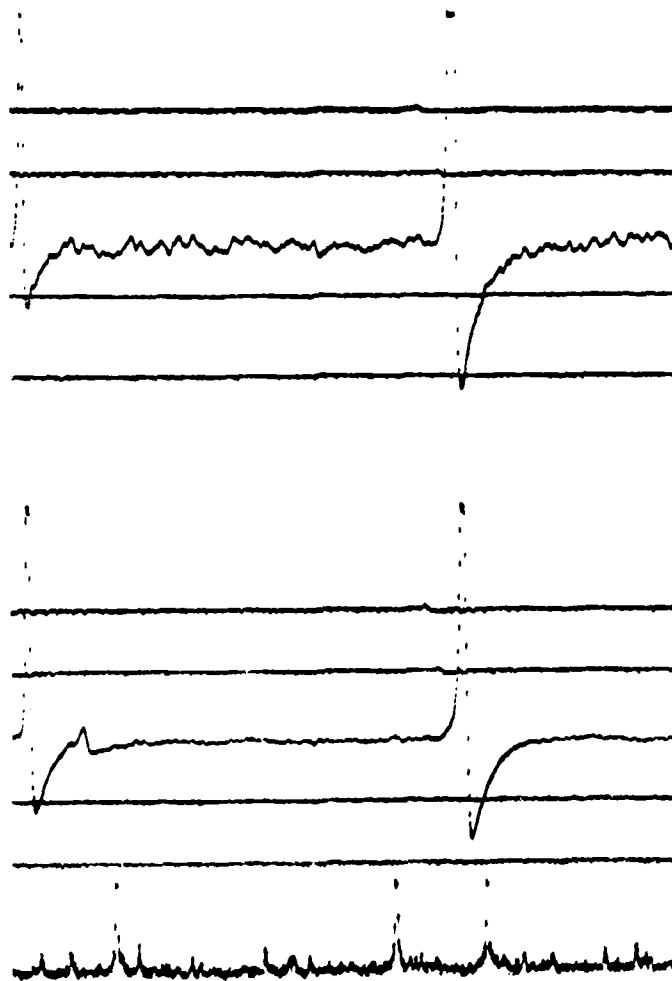


Figure 16. Transit and Signals From NGC 2183 and 2171

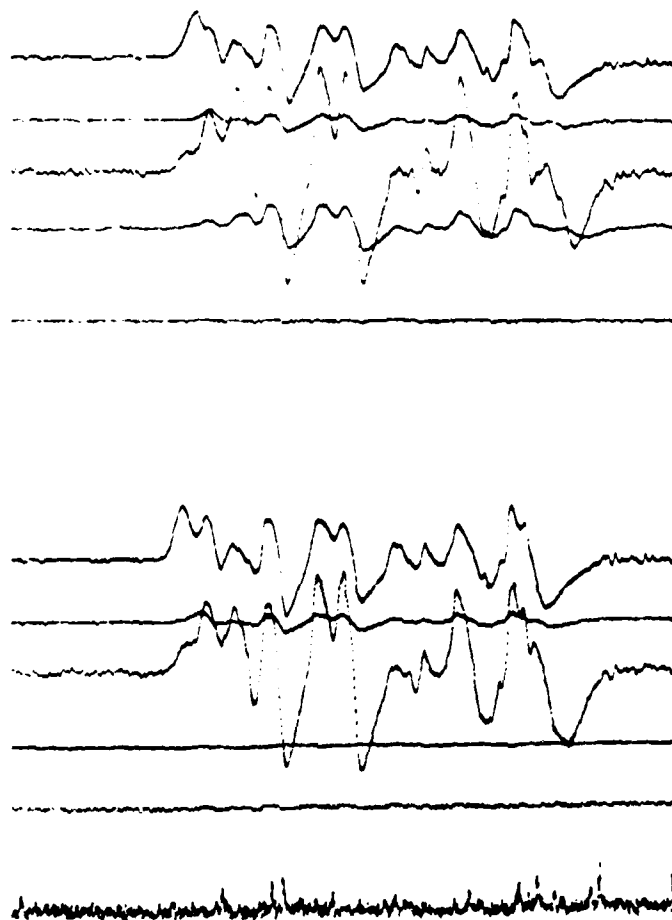


Figure 17. Signals From Optical Contamination. The characteristics double humped signature due to the out-of-focus image from the Gregorian optical system is evident

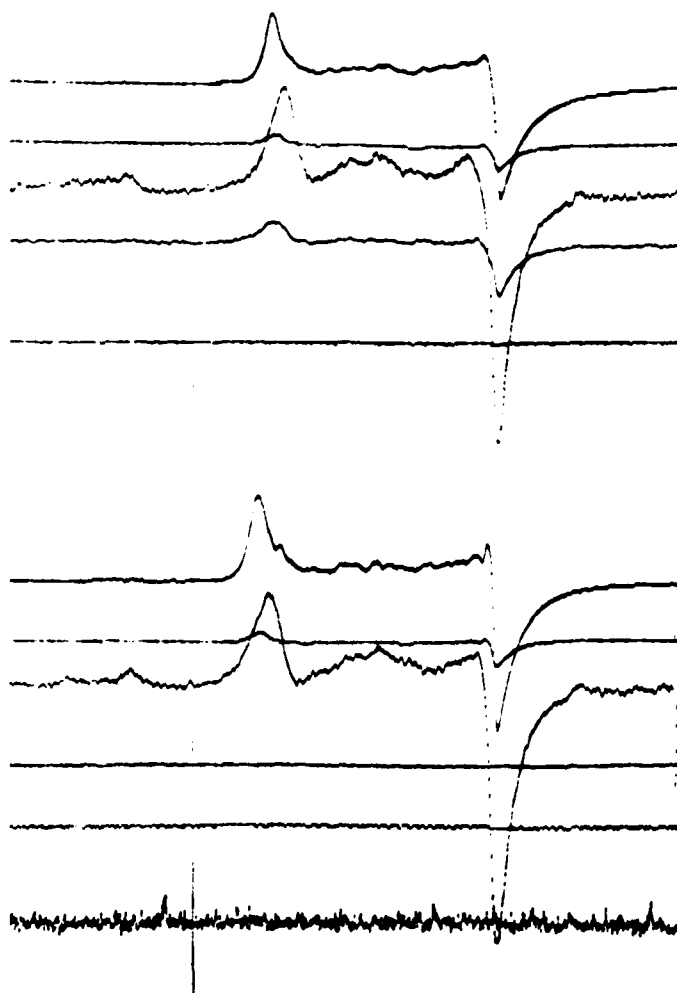


Figure 18. Response From an Extended Source of Nearly Constant Brightness

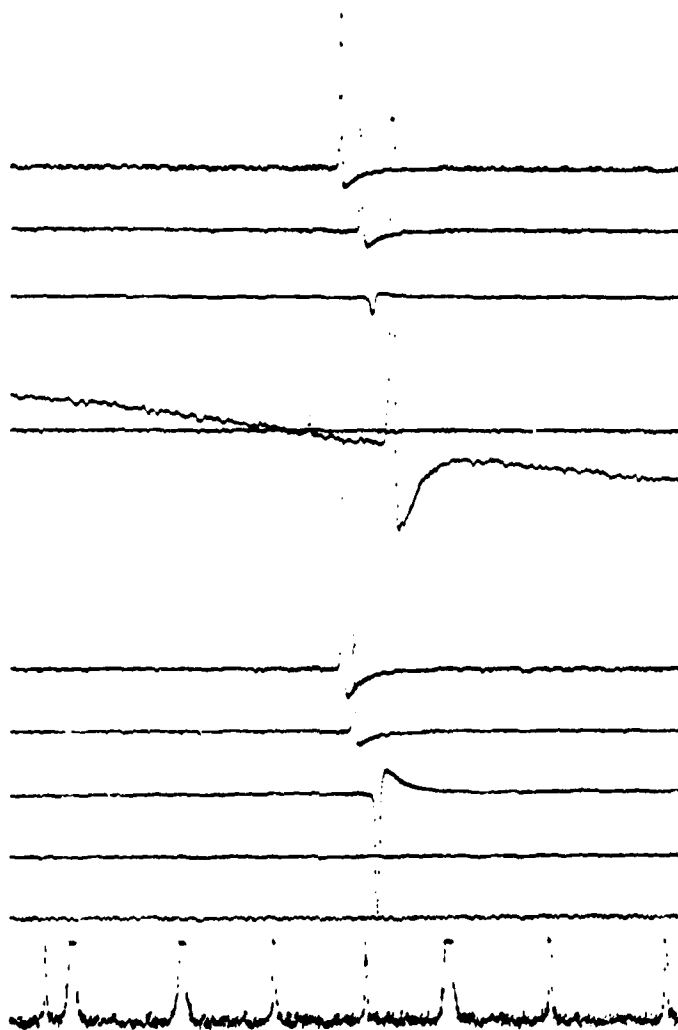


Figure 19. Signals From Saturn. The negative signals on the $11\text{ }\mu\text{m}$ detectors are due to bias reversal at the elevated focal plane temperatures

6. DATA REDUCTION - CALIBRATION

The in-flight calibration was based on the observations listed in the "Catalog of Infrared Observations" (CIO)¹⁴ augmented by measurements of Grasdalen et al., Nev and Merrill, and Rudy et al.^{15, 16, 17, 18} Measurements which exhibit, or are suspected of having, a beam size dependency were rejected. The calibration sources for the 20- μ m band were selected from those remaining listings which had a measurement between 18 and 23 μ m. The observations were converted to radiance then scaled to the FIRSSE reference wavelength (20.3 μ m), by a $\lambda^{3.95}$ power law. Multiple observations on a given source were averaged, and the amplitude of variation is noted. The same procedure is used for selecting the calibration sources and reference radiances for the 27.3- μ m band, except that the wavelength selection criterion was $20 < \lambda < 35 \mu\text{m}$.

The calibration objects in each color are associated with the FIRSSE detections by positional agreement. A weighted linear least squares regression with fixed intercept of zero is calculated for each detector channel. The calibration radiance values are given weights according to an estimate of the photometric quality of the observation and the amplitude of variability. Measurements are rejected if they deviate more than two standard deviations from the fit except if the FIRSSE detection falls in the overlap region of an adjacent detector. These measurements are rejected if they are of more than one sigma deviation.

Eight sources on the average, were used to calibrate each of the 20 μ m detectors. The 27.3 μ m calibration was not as straightforward since very few sources in the CIO meet the criteria for calibration objects at this wavelength. Further, most of the CIO measurements which qualify are at wavelengths shorter than 27.3 μ m and assuming a zero color difference will underestimate fluxes from sources with circumstellar emission. Five asteroids (2 Pallas, 8 Flora, 15 Eunomia, 54 Alexandra and 704 Internamnia) were used in the calibration. The color temperature of these objects were derived from the 10 and 20 μ m photometry by Morrison.¹⁹ The 27- μ m fluxes for the asteroids are extrapolated by scaling the color temperature derived from the 10 and 20 μ m photometry by the sun to asteroid distances at launch epoch and the time of the ground based observations then scaling the radiance by the earth to asteroid differences. Where comparisons could be made no significant differences were found between the responsivities derived from the CIO sources and the asteroids.

(Due to the large number of references cited above, they will not be listed here. See References, page 51.)

Even with the asteroid observations not enough sources were available to calibrate each of the 27- μm detector channels separately. Responsivities scaled from the NOSC measurements were also included. The final calibration for each detector were averages of the scaled NOSC values and the CIO sources. Thus, the greater the number of CIO objects the heavier the calibration is weighted with celestial sources. In general, the resulting responsivities agree with the laboratory measurements by NOSC and SBRC. The minimum flux for a source used in the calibration is about $10^{-17} \text{ W cm}^{-2} \mu\text{m}^{-1}$ with the majority of objects 5 to 10 times brighter. Most of the scatter in the regressions are due to the intrinsic variability in many of the sources used in the calibration.

The calibration of the two long wavelength bands was more complicated. There are very few valid standards at these wavelengths, and most objects have pronounced beam size flux dependencies. Further, the detector responses changed as a function of focal plane temperature. The post flight calibrations including varying the focal plane temperature between 3.2 and 4.5°K in steps of 0.05°K and recording the amplitude of the response of each detector to the internal stimulator. This calibration is used to correct the temperature dependence of the in-flight instantaneous response to values normalized to those at 3.2°K. Next it was assumed that the internal stimulators uniformly illuminate the Ge:Ga and Ge:Be arrays located in the middle of the focal plane. The detector to detector relative response in each of these arrays was determined from the response to the stimulator at 3.2°K. The calibration for the 94- μm array is the relative response scaled by an average of five objects used as standards at these wavelengths. AFGL 618 and AFGL 915 were extrapolated along the spectral distribution defined by published photometry at 33 and 53 μm ,^{20, 21} OH 0739-618, by 33 and 73 μm photometry,¹⁹ AFGL 490 by the 50 and 100 μm photometry.^{19, 22} Finally, the 30 μm fluxes in Gazari et al.¹⁴ for α Ori were extrapolated to 93 μm assuming a $\lambda^{-3.95}$ power law. The band averaged responsivities of the 40- μm array was scaled from the averaged in-flight response of the 27- μm array by the ratio of the array response determined at SBRC. Uncertainties in the calibration are estimated to be 10 to 15 percent at 20 μm , 15 to 20 percent at 27 μm and about 40 percent at the two longest wavelengths.

20. Kleinmann, S.G., Sargent, D.G., Mosley, H., Harper, D.A., Lowenstein, R.F., Telesco, C.M., and Thronson, H.A. (1978) Astron. Astrophys. 65:139.
21. Westbrook, W.E., Becklin, E.E., Merrill, K.M., Neugebauer, G., Schmidt, M., Willner, S.P., and Wynn-Williams, C.G. (1975) Observations of an isolated compact infrared source in Perseus, Astrophys. J. 207:407.
22. Harvey, P.M., Campbell, M.F., Hoffman, W.F., Thronson, H.A., and Gatley, I. (1979) Infrared observations of NGC 2071 (IRS) and AFGL 490: Two low luminosity young stars, Astrophys. J. 229:990.

7. DATA REDUCTION

The data reduction procedures are schematically shown in Figures 20, 21 and 22. The signals generated by the background as the detector sweeps across the sky are amplified and band limited. The high frequencies are limited by a low pass filter which is a two pole RC filter with a characteristic frequency of the inverse of twice the dwell time. These values are 250 Hz for the silicon arrays and 180 Hz for the Ge arrays. Thus, each color has a different upper band limit set by the various detector widths at a linear scan rate of 20 deg sec^{-1} . Low frequency signals due to off-axis response are attenuated by a single RC high pass filter set at 10 Hz. The signal is sampled and digitized by a pulse code modulation (PCM) unit. Gains for the amplifiers were set in the laboratory such that the rms noise is about one digitization level of the PCM unit.

As seen in Figure 20, the data is telemetered to the ground as it is gathered. On the ground, the PCM stream is recorded on analog magnetic tape and, in parallel, decommutated, converted from digital to analog and displayed on paper strip charts for quick look analysis. Post flight processing includes decommutating the analog tapes and packing the PCM digital data stream on digital computer tapes.

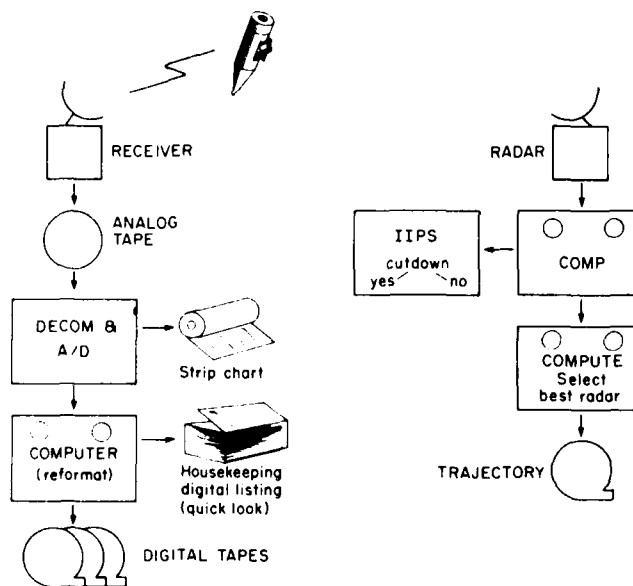


Figure 20. Data Acquisition for the Experiment

These tapes constitute the raw data for the experiment. Also, engineering performance of the experiment, for example, sensor temperature, is listed. Radio tracking during the flight provides a trajectory.

The digital tapes are processed to extract potential source signals and to calculate sensor aspect of azimuth and zenith angle with respect to the pole star as a function of time. The aspect is used to assign position to each potential source. Detections in more than one color are combined by position coincidence. Associations are made with known or suspected bright IR sources, asteroids and near earth satellites. Associations with sources in the CIO provide a list for photometric calibration. Sources which were confirmed by rescan are given a higher weight, and then a more stringent selection criterion is used to generate the final source list. This procedure is detailed in Figure 21.

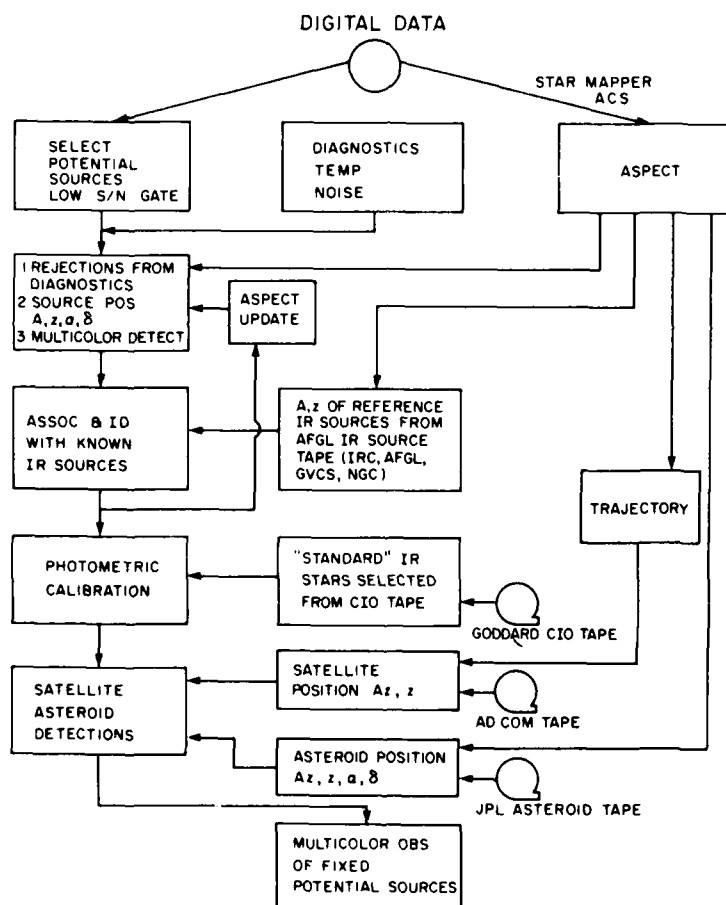


Figure 21. Flow Chart for Reduction of the Data and Association With Known Sources

A more detailed flow chart on selection of sources from the raw data stream is given in Figure 22. The central point is that two selection criteria are used in parallel. An average and rms noise level is calculated from the raw data. A potential source is selected if the signal exceeds three times the noise level above the average. This will detect objects which range from point sources to extended objects about a degree across. How large an extended source depends on the spatial intensity distribution, scan rate and the high pass filter. Reference to Figures 15 through 19 show that this procedure does not have good resolution downstream of large signals.

The data stream is also filtered by comparing the signal to the output two detector widths on either side of it. The result is convolved with the idealized filtered response to a point source. Then, a potential source is selected if the instantaneous signal is greater than three times the rms level of the noise and the cross correlation coefficient is determined. This routine strongly emphasizes the detection of point sources.

8. THE FIRSSE LONG WAVELENGTH CATALOG

Table 2 catalogs the FIRSSE long wavelength observations. The right ascension and declination for 1950 epoch is given in columns 1 and 2 and their respective errors in columns 3 and 4. The galactic longitude and latitude are listed in columns 5 and 6 respectively. The 20, 27, 40 and 94 μm fluxes are given in the next four columns in terms of Janskys ($1 \text{ Jy} = 10^{-26} \text{ W m}^{-2} \text{ Hz}^{-1}$). Associations of the source with other cataloged objects are given in column 11 while comments on the source are listed in the final column. Comments consist on whether the object is suspected (EO?) or measured to be extended (EO) and confirmed by rescan (R).

The thermal variations of the focal plane during the experiment produced considerable problems in the 40 μm band. The fluxes in these bands are indicative only.

The catalog contains 295 sources, the majority of which are associated either with optical HII regions or luminous stars embedded in dust clouds of circumstellar dust cells. Except for Mars and Jupiter, which are not included in the catalog, these sources comprise the list of 48 objects brighter than 1000 Jy at 93 μm . At the fainter levels stars begin to contribute to the list. In addition to the objects such as T Tau, VY CMa and U Mon which are associated with dust, the brighter photospheric radiators (α Ori, R Aur, α Boo and RX Boo) were detected. It should be noted that the effective wavelength of the 93- μm band shifts to about 74 μm if a λ^{-4} source function is convolved with the spectral response. Thus, the fluxes for photospheric radiators in the catalog are about a factor of two larger than they should be at 93 μm .

Additionally, the catalog contains three planetary nebulae and eight galaxies. The galaxies are

NGC 2146	Spiral (Type Sbc pec)	NGC 4666	Spiral (Type Sc)
NGC 4038	Seyfert	NGC 4736 (M 94)	Spiral (Type Sb)
NGC 4254 (M99)	Spiral (Type Sc)	NGC 5023	Marginal Detection
NGC 4631	Spiral (Type Sc)	NGC 4631	Spiral (Type Sc)

All of these are bright ($M_{\text{pg}} < 11.5$).

The sources observed at 93 μm are plotted on an Aitoff equal area all sky projection in Figure 23. The heavy lines define the boundary of the survey, the dashed line the galactic plane.

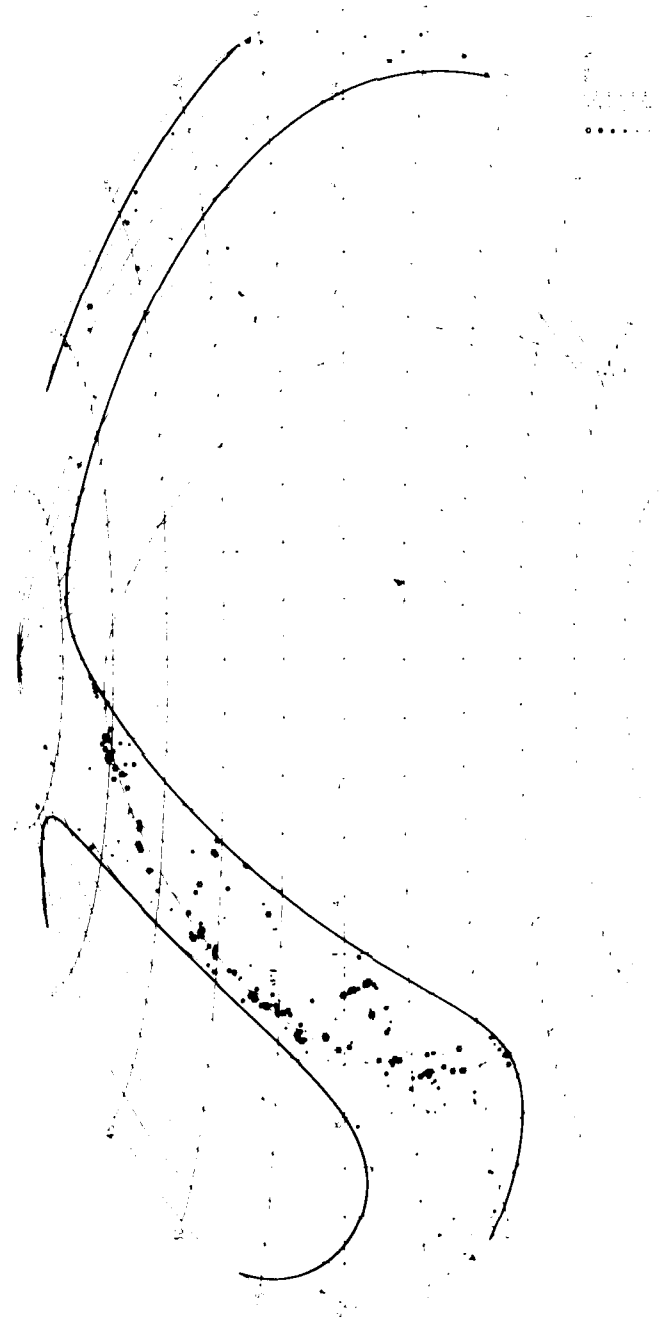


Figure 23. Aitoff Projection of the FIRSE Coverage and Sources Detected at 3 μ m

Table 2. Table of Observations

RA(1950)	Dec(1950)	EA	ED	l	b	(F20)	F(27)	F(40)	(F93)	Associations	Comments
0 ^h 36 ^m 26 ^s	+66°35.0	14 ^s	8.1	122	4				168		
0 37 33	+66 39.6	15	8.5	122	4				73		
0 40 39	+66 34.7	14	8.2	122	4				56		
0 46 44	+65 26.1	13	7.6	123	3		145		169		EO
0 48 28	+65 31.8	7	4.2	123	3			297	188		EO
0 51 46	+65 34.5	7	3.9	123	3				147		
0 55 20	+65 22.4	7	4.3	124	3				169		
1 2 36	+75 58.7	13	14.6	124	13				73		
1 4 29	+65 4.4	4	2.7	125	3	59	117		323		R
1 13 33	+64 36.4	4	2.6	126	2	25	53		113		EO*
1 20 0	+61 37.2	6	3.3	127	1	33			834	Sharp, 137, AFGL 205	EO
1 30 14	+62 10.8	4	2.6	128	-0	139	171		45	AFGL 230	R
2 3 29	+73 23.6	10	13.8	128	12	29		1091			EO
2 4 24	+60 31.2	4	2.4	132	-1	66	138		346		
2 13 5	+55 8.5	8	4.7	135	-6	19			49		
2 18 57	+57 35.3	13	8.0	135	-3				150	AFGL 4188S	EO
2 19 24	+61 38.7	4	2.9	134	1	42	49		344		EO
2 21 55	+61 51.6	2	1.6	134	1	3932	13, 681	11, 959	>27, 941	W3, AFGL 326	R
2 22 56	+61 21.8	5	4.1	134	1	30	56		332		R
2 23 22	+62 3.1	4	3.0	134	1	1417	372		1479	W3N, AFGL 328	EO
2 23 37	+61 40.1	3	2.5	134	1		1209		>33, 437	W3OH, AFGL 331	EO
2 24 40	+60 40.4	6	4.4	134	0	19			93		EO
2 24 55	+61 17.6	4	3.4	134	1	91	115		11, 454	AFGL 333	EO
2 38 1	+59 23.2	10	7.9	136	-0				135	Sharp, 197	EO
2 38 43	+53 18.4	10	6.6	139	-6				237		
2 39 1	+62 42.9	4	3.3	135	3	58	91	404	389		R
2 43 29	+61 45.3	6	6.0	136	2		48		244	Sharp, 192	R
2 45 44	+60 28.6	7	5.8	137	1	61	82	259	756		EO
2 46 1	+59 30.0	6	4.3	137	0				316	Sharp, 198	EO
2 46 2	+61 46.5	3	2.3	136	2	76	127		342		

Table 2. Table of Observations (Contd)

RA(1950)	Dec(1950)	EA	ED	l	b	F(20)	F(27)	F(40)	F(93)	Associations	Comments
2 ^h 46 ^m 40 ^s	+55 40.4	13 ^s	7.8	139°	-3°				169	η Per, AFGL 382	EO
2 47 27	+60 30.6	7	4.5	137	1				644	V400 Cas, AFGL 4026	EO
2 53 13	+60 8.8	1	0.9	138	1	58	63	347	893	LW Cas	EO
2 53 52	+60 35.8	9	8.3	138	2	22			690		EO
2 57 39	+60 17.3	2	2.0	138	2	157	202	262	>5866	LX Cas, AFGL 4029	EO
2 59 0	+60 14.5	3	2.9	138	2	174	240		>3366	Sharp, 201, AFGL 416	EO
3 3 37	+58 19.1	2	1.5	140	0	299	388	612	1609		R
3 3 51	+55 36.5	9	7.2	141	-2				70		EO
3 6 36	+56 38.9	3	2.1	141	-1	30	67	526	804		EO
3 21 6	+54 47.1	6	5.5	144	-2	40	119	857	701		EO
3 23 24	+58 35.7	3	2.4	142	2	185	363	508		AFGL 490	EO
3 25 34	+31 1.3	11	4.6	158	-21				272		R
3 26 10	+31 12.3	3	1.1	158	-20	124	101		774	SVS 6046, NGC 1333	EO
3 41 21	+31 57.9	2	1.0	161	-18	46	66	93	>1722	IC 0348	EO
3 41 52	+23 58.4	10	4.2	166	-24	27			66		EO
3 42 11	+23 36.2	11	4.3	166	-24				39	Or Tau	EO
3 42 41	+24 11.5	10	4.3	166	-24	18			134	SVS 100311	EO
3 42 48	+31 22.1	10	4.7	161	-18				639		EO
3 43 8	+23 39.6	12	5.3	167	-24	25	40		425	OW Tau, NGC 1435	EO
3 43 40	+24 17.7	6	2.3	166	-23				36	V638 Tau	EO
3 45 2	+65 22.6	2	3.4	140	9	45			36	AFGL 520	R
3 51 53	+37 12.1	12	5.6	159	12				194		EO
3 52 19	+53 43.5	3	2.2	148	0	24			203		R
3 59 34	+51 11.6	2	1.5	151	-1	167	267		1105	Sharp, 206	EO
4 7 22	+51 2.3	1	1.2	152	-0	499	611	1634	>11,655	Sharp, 209, AFGL 550	EO
4 15 32	+28 12.0	3	1.2	169	-16	91	73		396	CZ Tau	EO
4 19 9	+19 25.4	4	1.7	176	-21	46	72		42	Tau, Sharp, 238	EO
4 27 4	+35 10.2	2	1.1	165	-9	337	1150		>3988	Sharp, 222, AFGL 525	EO
4 28 43	+18 2.1	4	1.4	179	-20	47	106		2019	Sharp, 239	EO
4 32 31	+51 6.7	1	1.1	154	3	57	151	217	1474		R

Table 2. Table of Observations (Contd)

RA(1950)	Dec(1950)	EA	ED	l	b	F(20)	F(27)	F(40)	F(93)	Associations	Comments
$4^{\text{h}}33^{\text{m}}7^{\text{s}}$	$+50^{\circ}46'6''$	3 ^S	3.8	155°	2°	33	78		984	Sharp, 211	R
4 36 56	+50 22.3	2	1.7	155	3	70	96		1555	NGC 1624	R
4 39 31	+36 1.1	2	1.4	166	-7	1006	1102	450	434	AFGL 618	
4 52 26	+47 16.8	5	6.2	159	3	20			188	Sharp, 219	
4 54 52	+47 53.9	5	6.3	159	3		116		623	Sharp, 217	
4 56 38	+56 6.5	1	1.9	153	9	1060	608		19	1 x Cam, AFGL 664	R
5 4 18	-3 26.8	3	0.8	204	-25	42	112	311	1221	NGC 1788	EO R
5 9 55	+37 23.1	2	1.6	169	-1	64	99		189	Sharp, 228	R
5 13 11	+34 16.8	2	0.9	172	-2	81	94		109	AE Aur, IC 0405	EO R
5 13 26	+45 31.0	2	1.8	163	4	45	51			AFGL 712S	R
5 13 26	+53 31.8	1	5.0	156	9	142	86		9	R Aur, AFGL 715	R
5 19 42	+33 55.5	2	0.6	173	-1	26	45		1493		R
5 19 56	+33 29.2	5	3.5	174	-2	30	118		128	NX Aur	EO ⁹
5 22 11	+41 39.9	4	4.9	167	3		68		43		R
5 23 49	+34 7.4	4	2.4	173	-1	52	44		100	S Aur, Sharp, 234, AFGL 748	R
5 24 43	+34 22.1	2	1.6	173	-0	43	78		571	SVS 102471, IC 0417, AFGL 4415S	EO R
5 27 26	+33 45.9	3	2.1	174	-0	39	127		390		
5 28 7	+34 13.9	3	1.9	174	0	114	226	1564	1322	NGC 1931	EO ⁹
5 30 20	+59 11.3	3	4.3	153	14	94			15		R
5 30 20	-5 31.2	1 ²	3.6	209	-20				849	V466 Ori	
5 30 23	+30 28.3	5	3.3	177	-1	42	139		158		
5 31 32	+21 59.2	4	1.4	185	-6	36	61		54	Cam Tau, NGC 1952	R
5 32 25	+57 23.1	3	5.5	155	13	60			53		R
5 32 32	-6 8.1	13	210	-20					479	V788 Ori, AFGL 442aS	
5 32 40	-4 44.2	13	3.6	208	-19				1171	SVS 6251, NGC 1973	
5 32 46	-4 52.5	3	0.9	208	-19	92	431		4792	SVS 6282, NGC 1977, AFGL 781	EO R
5 32 50	-5 24.6	4	0.9	209		>30, 489	>29, 454	>29, 312	>15, 893	M42, NGC 1982, AFGL 779	EO R
5 32 52	+36 28.8	5	2.4	173	2	20	217		133		EO R
5 33 22	-4 16.4	9	2.5	208	19		168	12, 694	8992	567 Ori	
5 33 46	-5 19.1	15	4.3	209	-19					V 853 Ori	EO

Table 2. Table of Observations (Contd)

RA(1950)	Dec(1950)	E.A.	E1	1	b	F(20)	F(27)	F(40)	F(63)	Associations	Comments
5 33 53 ^S	-30°28.3	7 ^S	1.8	210°	-20°				212	V380, Ori, NGC 1969	R
5 34 36	-31 58.1	3	2.1	177	0	19			405	NGC 1985	EO
5 35 0	-4 56.6	10	2.6	209	-18	59			315	SVS 100651	EO
5 35 11	-35 50.1	3	1.6	173	2	24	58	307	313		EO
5 35 33	-30 40.4	4	2.2	178	0		76		354		EO
5 36 11	-46 44.5	2	4.3	164	8	190	113		27	DO 25520, AFGL 791	R
5 36 23	-36 1.6	3	2.2	173	3	26			175		R
5 37 7	-36 21.3	7	5.2	173	3				259		R
5 37 10	-35 48.8	4	3.8	174	3	186	260	939	22636	Sharp, 233	EO
5 37 41	-35 40.8	5	3.7	174	3		393	2888	292		EO
5 37 55	-7 30.4	5	1.2	212	19	79	131		121	V902 Ori	R
5 37 55	-3 23.2	10	2.6	208	17	13			35		EO
5 37 58	-1 59.3	5	1.4	206	-17	34			682	ζ Ori	EO
5 38 16	-35 48.3	5	3.7	174	3	44	290		480	Sharp, 235	EO
5 39 1	-2 18.4	5	1.3	207	-17	176			2809	SVS 6365, NGC 2073, AFGL 805	EO
5 39 14	-1 56.6	11	3.1	207	-16	7142	14,453	17,000	5561		R
5 40 33	-32 41.3	2	1.2	177	2	183	130		21	AFGL 805	R
5 40 59	-30 55.0	3	1.8	178	1	29			46	FP Aur	R
5 41 24	-1 17.8	13	3.5	206	16				425		EO
5 44 2	-0 2.3	3	0.7	205	14	133	345	1021	4299	SVS 6369, NGC 2064, AFGL 8148	EO
5 44 6	-30 34.5	3	1.8	179	1				32	FP Aur	EO
5 44 31	-0 17.6	3	0.9	205	14	247	485	500	1723	SVS 653, NGC 2073, AFGL 817	EO
5 58 3	+25 45.2	4	2.0	183	-1		27		318		EO
5 48 0	-27 1.8	6	3.3	182	0				52		R
5 49 2	-27 0.2	2	1.1	182	0	29	75	628	491	SLC 212	EO
5 50 17	-24 14.3	2	1.0	185	1	54	70		49	R6 Tau	R
5 52 25	-7 23.3	2	0.7	200	9	2722	1141	444	243	α Ori, AFGL 836	R
5 55 17	-16 41.2	7	2.8	182	4	54	115		393		R
5 55 25	-20 13.4	3	1.2	189	2	50	36		310		EO
5 57 16	-21 56.4	5	3.4	179	4	45			41		R

Table 2. Table of Observations (Contd)

RA(1950)	Dec(1950)	EA	ED	l	b	F(20)	F(27)	F(40)	F(93)	Associations	Comments
$6^h 0^m 26^s$	$+75^\circ 43' 6''$	11 ^s	15.7	138°	24°				49	AFGL 4470S	
6 0 46	-30 15.3	2	1.4	181	44	38	54		499	Sharp. 241	EO R
6 1 15	-30 29.8	1	0.1	181	4	75	65		426		EO
6 1 18	-30 40.9	6	1.5	216	-15	16			328	NGC 2149	EO ² R
6 4 15	-21 14.9	10	4.3	189	0				76		
6 5 18	-6 22.6	3	0.8	214	-13	2275	5866	12, 976	> 18, 825	NGC 2170, AFGL 877	EO R
6 5 21	-20 38.2	7	3.0	190	0	117	150		724		EO R
6 5 42	-21 31.0	11	5.3	189	1	118			1218		
6 5 55	-21 37.8	7	3.0	189	1		152	1034	-2284	Sharp. 247	R R
6 5 59	-15 41.5	5	1.9	194	-2	34			306		EO R
6 6 24	-20 41.5	3	1.2	190	1	148	296		> 1307		EO R
6 6 58	-20 30.9	11	5.2	190	1	74	132		> 1876	Sharp. 252	EO
6 7 14	-21 41.8	11	4.4	189	1				108		
6 7 22	-12 49.4	4	1.3	197	-3	66	204		493	Ef Ori, Sharp. 270	R
6 7 27	-16 43.7	6	2.1	193	-1				71		EO R
6 8 3	-20 28.6	13	4.7	190	1				365		EO
6 8 18	-6 13.0	9	2.3	213	-12	555	972		-3278	NGC 2183, AFGL 890S	R
6 8 18	-20 39.6	13	4.7	190	1				723		EO
6 8 37	-17 28.5	5	1.8	193	-1				94	Sharp. 259	R
6 8 42	-21 3.8	10	4.3	190	1				87		
6 8 58	-20 39.2	10	4.2	190	1				126		
6 9 1	-17 55.6	9	3.1	193	-0				110		EO R
6 9 13	-6 12.5	10	2.4	2.4	-12	24	73	182	141		EO?
6 9 33	-78 24.7	5	8.2	136	25				98	NGC 2146	
6 9 42	-62 36.7	10	9.4	152	20				218		EO
6 9 56	-18 0.5	2	0.7	193	-0	325	646	6107	-3639	Sharp. 257, AFGL 896	EO R
6 10 11	+18 47.0	11	4.1	192	0				49		EO
6 10 19	+15 23.0	5	1.9	195	-1	39	93		287		R
6 10 43	-17 58.6	7	2.5	193	0	47	33		236	Sharp. 258	EO R
6 10 56	-18 44.6	11	4.1	192	1				51		

Table 2. Table of Observations (Contd)

RA(1950)	Dec(1950)	EA	ED	l	b	F(20)	F(27)	F(40)	F(93)	Associations	Comments
6 ^h 11 ^m 31 ^s	+17°46'0	3 ^S	1:2	193°	0°	43	83		512	NGC 2195	R
6 11 32	+13 52.1	8	2.7	196	-2	133	258		2926	Sharp, 269, AFGL 902	R
6 11 53	+19 1.4	7	2.6	192	1		137		137		
6 12 3	+19 5.0	10	4.1	192	1	21			509		
6 12 7	+12 21.3	1	0.3	198	-2	30	53		348	Sharp, 271	EO R
6 12 47	+14 16.3	5	1.7	196	-1	30	104		244	Sharp, 267	
6 13 39	+15 58.3	14	3.3	224	-15	87	134		29		EO
6 15 40	+23 20.7	8	4.2	189	4	28	78		488	Sharp, 266	EO R
6 15 50	+13 17.3	3	1.0	196	-0	416	324		360	AFGL 915	EO R
6 17 32	+10 37.3	4	0.9	219	-12				66		
6 18 35	+66 18.2	4	3.4	148	22	431	290		49		EO
6 20 53	+9 58.6	8	2.6	201	-2	18			211		R
6 24 49	+10 9.7	11	2.4	219	-10	36	47		159		R
6 26 50	+8 49.7	9	2.5	203	-1	41			25	V 477 Mon	R
6 28 13	+13 18.3	8	2.7	199	2	15			75		
6 28 20	+9 35.3	5	1.2	219	-9	32			820		EO R
6 28 23	+9 52.8	6	1.6	202	-				238	V 479 Mon, IC 2169	EO R
6 28 23	+10 29.5	4	1.2	201	0	93	78		163	V 540 Mon, IC 2167, AFGL 951S	
6 28 53	+10 2.4	9	2.6	202	0	12			34	V 483 Mon	
6 29 14	+4 22.4	9	2.4	207	-2	19			1615		R
6 30 0	+10 12.3	4	1.2	202	1	25			131	SVS 102513, NGC 2245	R
6 30 24	+10 23.5	5	1.6	202	1	27			165	V 490 Mon, NGC 2247	EO R
6 30 43	+10 59.3	9	2.6	201	1				44		R
6 30 59	+4 3.4	3	0.9	207	-2	42	93		1331		EO R
6 31 59	+4 15.3	9	2.4	207	-2	293	300		4015	AFGL 961	EO R
6 33 1	+11 1.8	9	2.5	201	2				123		R
6 33 52	+10 50.3	4	1.2	202	2	22	49		580		EO R
6 33 58	+10 27.1	6	1.8	202	2				85		EO R
6 33 56	+1 36.1	1	0.3	213	-4	17	55		58	CY Mon	R
6 36 27	+8 47.0	3	0.8	204	1	102	109		83	R Mon, NGC 2261	R

Table 2. Table of Observations (Contd)

RA(1950)	Dec(1950)	EA	ED	l	b	F(20)	F(27)	F(40)	F(93)	Associations	Comments
$6^h 37^m 12^s$	$+10^\circ 40' 9''$	13 ^s	3:7	202 ^s	2 ^s				73		
6 38 0	+9 51.3	4	1.0	203	2	34	72		1188	V425 Mon, NGC 2264, AFGL 4519S	EO R
6 38 10	+10 39.3	6	1.7	202	3				168		EO R
6 38 28	+10 3.1	9	2.6	203	2	41			57	V609 Mon	EO R
6 38 30	+9 33.4	2	0.6	203	2	271	322	832	1824	CV Mon, AFGL 989	EO R
6 41 19	-1 4.8	2	0.6	213	-2	96	174		856		EO R
6 42 59	-16 39.3	10	2.1	227	-9	40				α CMa, AFGL 1007	R
6 44 15	+1 20.5	10	2.2	211	-0	35	49		1565	V507 Mon, NGC 2282	R
6 50 0	+8 28.7	2	0.5	206	4	559	445		51	GX Mon, AFGL 1028	R
6 55 52	-13 58.3	15	2.7	226	-5	346	260		18		R
6 56 16	+3 39.1	10	2.3	211	3	32			23		
6 57 21	-7 40.8	10	2.0	221	-2	108	199		697	NGC 2316	R
6 59 26	-11 13.4	9	1.6	224	-3	26		481	1037	Sharp, 293	R
7 1 21	-11 29.2	3	0.6	225	-3	176	178		373	Z CMa, AFGL 1059	EO R
7 1 47	-11 13.8	4	0.8	224	-2	61	110		316	NGC 2327	R
7 2 1	-10 22.6	3	0.5	224	-2	53	87	366	550	SVS 102541	EO R
7 2 57	-12 14.5	2	0.4	225	-3	60	142		1448	Sharp, 297	EO R
7 6 53	-10 47.2	9	1.5	225	-1	38	71		193		EO R
7 7 43	-18 26.9	5	0.9	232	-4	63	58		531	Sharp, 301	EO R
7 9 9	-19 44.9	4	0.7	233	-5	49	67		86		R
7 9 57	-20 11.0	5	0.9	233	-5	71	58		51	AFGL 1085	EO R
7 14 11	-9 20.6	15	2.7	224	1	32			258	Sharp, 294	EO R
7 15 54	-21 59.7	11	1.9	236	-4	24			29		
7 20 55	-25 39.8	3	0.6	239	-5	933	7260	6652	1406	VY Cma, AFGL 1111	EO R
7 27 28	-17 45.1	18	3.4	233	0				77		EO
7 27 39	-18 4.8	16	2.5	233	-0				54		
7 27 58	-18 28.6	5	0.9	234	-0	138	257		1001	RCW 8	EO R
7 28 7	-17 49.7	16	2.5	233	0				78		
7 28 25	-15 10.4	16	2.4	231	2	25			120	Sharp, 299	
7 28 27	-9 38.8	4	0.7	226	4	77	61		48	U Mon	R

Table 2. Table of Observations (Contd)

RA(1950)	Dec(1950)	EA	ED	l	b	F(20)	F(27)	F(40)	F(53)	Associations	Comments
7 ^h 28 ^m 35 ^s	-17°34'6"	16 ^s	2.5	233°	0°				80		
7 29 40	-19 14.8	4	0.7	235	-0	28	58		518		EO R
7 29 51	-16 51.4	10	1.4	233	1	117	269	875	>1934	NGC 2409	EO R
7 31 14	-22 3.5	7	1.1	237	-1	34	83		94		EO R
7 31 14	-21 56.6	12	1.8	237	-1		60		461		
7 32 30	-22 16.3	16	2.5	238	-1				49		
7 33 21	-22 15.3	7	1.2	238	-1	18			161		R
7 33 22	-18 40.7	3	0.5	235	1	35	124	797	698	Sharp, 307	EO R
7 35 52	-32 44.8	6	1.0	247	-6	37	91		114		
7 38 23	-33 25.6	8	1.3	248	-5				112		
7 39 57	-14 36.9	11	1.5	232	4	343	666		433		R
7 42 15	-20 0.4	9	1.3	237	2				49		
7 42 47	-23 59.7	6	0.8	240	0	20	69	142	4069		EO R
7 45 0	-19 44.7	16	2.3	237	2				19		
7 43 42	-19 48.8	16	2.3	237	2				21		
8 43 49	-19 13.8	16	2.3	236	3				35		
7 48 30	-33 29.5	21	2.5	249	-4				54		
7 50 10	-25 48.7	18	3.0	243	1				118		EO
7 50 29	-26 16.1	3	0.5	243	0	182	257	2890	4186	NGC 2467	EO R
7 53 0	-34 44.3	17	2.3	251	-4				79		
7 53 25	-20 34.2	17	2.5	239	4				164		EO
8 0 42	-34 23.3	17	2.0	251	-2	33			99		
8 11 5	-33 9.5	4	0.6	251	1	147	137		30		R
8 11 15	-2 49.4	6	0.7	225	17		77		156		
8 13 7	-35 12.6	17	2.0	253	-0				33		
8 14 7	-35 58.4	17	2.0	251	-1				121		
8 14 51	-35 17.8	18	3.0	254	-0				142		EO
8 15 0	-35 27.1	18	3.0	254	-0				443		EO
8 16 1	-35 44.3	6	0.9	254	-0	32	87		216		EO
8 17 4	-21 35.1	3	0.4	242	8	172	151		47		R

Table 2. Table of Observations (Contd)

RA(1950)	Dec(1950)	EA	ED	l	b	F(20)	F(27)	F(40)	F(93)	Associations	Comments
8 ^h 19 ^m 3 ^s	-36° 41'	21 ^s	1:8	255°	0°	467	825		> 1435	NGC 2579	EO?
8 27 13	-28 9.5	17	1.6	249	6				94		EO
8 31 56	-35 53.5	18	2.7	256	2				734		
8 36 38	-27 53.1	17	1.5	250	8				75		
8 41 22	-28 3.0	17	1.4	251	9				66		
9 3 7	-5 36.2	17	0.9	235	26				49		
9 53 9	+75 51.7	17	5.5	135	37				151		
9 55 3	+75 59.1	17	5.7	135	37				62		
10 31 9	-28 48.8	17	2.0	269	24				138		
10 34 56	-28 51.1	12	1.4	271	25		56	411		V Hya, AFGL 1439	R
10 49 12	-20 59.2	11	1.4	269	34	541	291	714	60	R Cr, AFGL 1450	R
10 58 6	-18 4.1	11	1.5	269	37	391	202		39		
11 25 56	-28 12.8	16	2.9	282	31				137		
11 30 9	-27 33.1	16	2.9	282	32				22		
11 30 25	-23 46.0	11	2.0	281	35	26			26		
11 39 56	+ 4 15.4	7	1.7	265	62		160	325	44		EO
11 40 35	+ 4 12.9	17	4.0	265	62	319	447	1213	49		EO
11 41 36	+ 3 39.6	14	3.3	266	61			1009	28		EO
11 45 27	-27 27.4	15	2.9	286	33	62	200		21		EO
11 48 27	-21 56.9	15	3.0	285	39				38		
11 50 26	-22 37.9	15	3.0	286	38						
11 53 27	-24 52.2	8	1.6	287	36	20	88		17	SVS 1793	
11 59 18	-18 34.8	15	3.1	287	42				28	NGC 4038	
12 1 11	-26 8.3	4	0.8	290	35	5682	4280		467		
12 2 51	-21 45.1	18	3.6	289	40	3745	3203		455		EO
12 3 33	+16 51.6	11	4.0	256	75				92		
12 4 21	+17 8.8	11	4.0	256	75				370		
12 4 34	+16 58.0	11	4.0	256	75				116		
12 9 36	-13 54.9	18	3.8	289	48				120		

Table 2. Table of Observations (Contd)

RA(1950)	Dec(1950)	EA	ED	l	b	F(20)	F(27)	F(40)	F(93)	Associations	Comments
^h 12 ^m 16 ^s	+14°42'8"	12	3.9	270	75				49	NGC 4254	
12 27 51	+4 41.3	5	1.3	290	67	195	56		43	RR Vir, AFGL 1554	
12 36 13	-4 1.1	13	3.4	297	58				46	AFGL 4854s	
12 39 34	+32 47.6	5	3.5	143	84				77	NGC 4631	R
12 40 6	+60 18.5	10	8.9	125	57				80		EO
12 42 54	-11 0.3	10	2.5	301	52		63		109		EO
12 48 35	+41 22.8	2	1.9	123	76				107	NGC 4736	R
13 0 52	-8 47.5	13	3.5	308	54				87		
13 1 27	-8 38.2	15	3.8	308	54				386		EO ^a
13 10 13	+44 19.5	8	6.1	110	73				371	NGC 5023	EO
13 13 45	+42 17.9	6	5.7	106	74				36	NGC 5055	
13 21 51	+54 36.0	2	7.3	113	62	15			1433		EO
13 52 24	+56 8.7	4	7.6	106	59	187			111		EO
14 13 23	+19 25.9	7	2.9	15	69	197	82		53	α Boo, AFGL 1643	
14 21 49	+25 56.0	3	1.1	34	69	732	224		22	RA 1800, AFGL 1706	R
14 36 35	+44 46.5	6	4.2	79	62	20			425		
15 50 27	+58 56.0	9	7.9	91	46				63		
16 10 15	+66 29.4	7	7.2	99	40	36			26		
16 56 38	+65 11.5	14	10.0	96	36				429	SVS 101623	EO
17 58 31	+66 38.8	14	7.7	96	30	69	117		86	NGC 6543	
18 32 1	+69 9.1	15	8.3	100	27				105		
21 10 8	+81 29.3	17	5.3	115	22				30		
21 11 46	+73 15.3	17	2.5	109	17				39		
21 20 49	+77 40.7	12	1.6	113	19	39		2075		GH Cep, AFGL 2757	R
21 26 35	+73 23.6	17	2.7	110	16				108		
23 51 1	+75 50.3	15	11.4	119	14				29	TN Cep	

References

1. Houck, J. R., Fuhman, K., and Harwit, M. (1968) Far infrared observations of the night sky from above the atmosphere: Preliminary results, Astron. J. 73:599.
2. Feldmann, P. D., McNutt, D. P., and Shivanandan, K. (1968) Rocket observations of bright celestial sources in ura major, Astrophys. J. Letters, 154:L131.
3. Pipher, J. L. (1971) Rocket Submillimeter Observations of the Galaxy and Background, Ph. D. Thesis, Cornell University, CRSR 461.
4. Houck, J. R., Soifer, B. T., Pipher, J. L., and Harwit, M. (1971) Rocket infrared four color photometry of the galaxy's central region, Astrophys. J. Letters, 169:L31.
5. Soifer, B. T., Pipher, J. L., and Houck, J. R. (1972) Rocket infrared observations of HII Region, Astrophys. J. 177:315.
6. Bratt, P. R., and Lewis, N. N. (1977) Development of Doped-Germanium Photoconductors for Astronomical Observations at Wavelengths from 30 to 130 Micrometers, NASA-CR-152, 046.
7. Bratt, P. R., and Lewis, N. N. (1979) Continued Development of Doped-Germanium Photoconductors for Astronomical Observations at Wavelengths from 30 to 120 Micrometers, NASA-CR-152, 125.
8. Moore, W. J. (1979) Final Technical Report Part I, Gallium-Doped Germanium - Evaluation of Photoconductors, NRI Mem. 3939, NASA-CR-152, 222.
9. Price, S. D., Murdock, T. L., and Shivanadan, K. (1981) Air Force Geophysics Laboratory (AFGL), infrared sky survey experiment, SPIE, 280:33.
10. NOSC (1980) Test Data on SBRC FIRSSE Focal Plane Array, Infrared Devices Branch, Electronic Materials Sciences Division, Naval Oceans Systems Center, San Diego, CA 92152, May 1980.
11. Price, S. D., Murdock, T. L., McIntyre, A., Huffman, R. E., and Paulsen, D. E. (1980) On the diffuse cosmic ultraviolet background measured from ARIES A-8, Astrophys. J. Letters, 240:L.

References

12. Price, S.D., Cunniff, C.V., and Walker, R.W. (1978) Cleanliness Consideration for the AFGL Infrared Celestial Survey Experiments, AFGL-TR-78-0171, AD A060116.
13. Price, S.D., Akerstrom, D.A., Cunniff, C.V., Marcotte, L.P., Tandy, P.C., and Walker, R.G. (1978) Aspect Determination for the AFGL Infrared Celestial Survey Experiments, AFGL-TR-78-0253, AD A067017.
14. Gazari, D.Y., Schmitz, M., and Mead, J.M. (1982a) Catalog of Infrared Observations, NASA Tech Mem. 83819; (1982b) Far Infrared Supplement: Catalog of Infrared Observations, NASA Tech Mem. 84001.
15. Grasdalen, G.L., Gehrz, R.D., Hackwell, J.A., Castelez, M., and Gullixson, C. (1983) The stellar component of the galaxy as seen by the AFGL infrared sky survey, Astrophys. J. Suppl. (in press).
16. Nev, E.P., and Merrill, K.M. (1980) Study of Sources in AFGL Rocket Infrared Study, AFGL-TR-80-0050, AD A084098.
17. Rudy, R.J., Gosnell, T.R., and Willner, S.P. (1979) Ground-Based Measurements of Sources in the AFGL Infrared Sky Survey, AFGL-TR-79-0172, AD A081381.
18. Gehrz, R.D., Jackwell, J.A., and Grasdalen, G.L. (1979) Infrared Studies of AFGL Sources, AFGL-TR-79-0274, AD A084713.
19. Morrison, D. (1977) Asteroid sizes and albedos, Icarus, 31:185.
20. Kleinmann, S.G., Sargent, D.G., Moseley, H., Harper, D.A., Lowenstein, R.F., Telesco, C.M., and Thronson, H.A. (1978) Astron. Astrophys. 65:139.
21. Westbrook, W.E., Becklin, E.E., Merrill, K.M., Neugebauer, G., Schmidt, M., Willner, S.P., and Wynn-Williams, C.G. (1975) Observations of an isolated compact infrared source in Perseus, Astrophys. J. 207:407.
22. Harvey, P.M., Campbell, M.F., Hoffman, W.F., Thronson, H.A., and Gatley, I. (1979) Infrared observations of NGC 2071 (IRS) and AFGL 490: Two low luminosity young stars, Astrophys. J. 229:990.

END

FILMED

9-83

DTIC